Introduction of oxygen vacancy to $Bi_2Mn_4O_{10}$ supported by nickel foam for $^1O_2$ dominated metronidazole degradation under dielectric barrier discharge plasma

Tianyao Shen [a], Xiaojing Wang [c], Jiaqin Li [a], Peng Xu [a], Chunyan Yang [a], Peng Wang [a,*], Guangshan Zhang [b,*]

[a] State Key Laboratory of Urban Water Resource and Environment, School of Environment, Harbin Institute of Technology, Harbin 150090, PR China
[b] Qingdao Engineering Research Center for Rural Environment, College of Resource and Environment, Qingdao Agricultural University, Qingdao 266109, PR China
[c] School of Environment, Sichuan Agricultural University, Chengdu 611134, PR China

ARTICLE INFO

ABSTRACT

Antibiotics in surface water adversely affect food safety and aquatic ecosystem, which hinder biological water treatment, and advanced oxidation technology (AOPs) is of great significance. This study achieved nitro-imidazole antibiotic metronidazole (MNZ) removal in a dielectric barrier discharge plasma (DBDP) process. A ternary $Bi_2Mn_4O_{10}$/NiF (BMON) was synthesized via microwave-assistant to enhance the DBDP process. Compared with $Bi_2Mn_4O_{10}$, BMON has a more stable structure with lower ion dissolution but higher oxygen vacancy (Vö) content. The DBDP process generates active species, and O_2^- acts as an intermediate in forming $^1O_2^-$ to degrade MNZ through multipath. The cycle of lattice oxygen $(O_L)/O_2$ and $M^{n+}/M^{(n-1)+}$ maintain the charge balance on the BMON surface, during which the transformation of Vö and $^1O_2$ improve the catalytic efficiency. Furthermore, MNZ possible degradation pathways were proposed by DFT calculations and ESI-QTOF-MS detection. The DBDP/BMON process exhibited great potential for heterogeneous catalytic in nitroimidazole antibiotic degradation.

1. Introduction

Nitroimidazole antibiotics are a type of organic pharmaceutical with a 5-nitroimidazole ring structure. Based on the potency of antibacterial, anti-inflammatory, antiprotozoal, and antiviral effects, they are widely used in anaerobic bacterial and parasitic infections treatment. In addition, nitroimidazole compounds are used as additives in poultry and fish feeds [1,2]. Metronidazole (MNZ, $C_6H_9N_3O_3$) is a typical nitroimidazole antibiotic with high solubility in water (9.5 g L^{-1}, 25 °C). Studies have shown that nitroimidazole antibiotics have potential toxicological effects, including mutagenicity and carcinogenicity, and their resistance rate in microorganisms is increasing [3,4]. In addition, due to the character of penetrating the cell membranes of microorganisms, its reduction products in the microbial cell will destroy the middle of the microbial DNA [3]. Therefore, MNZ is difficult to effectively eliminate by traditional biochemical treatment technology in urban sewage treatment, bringing the potential risk of natural water pollution, threatening aquatic ecosystems and human health [4,5]. At present,

nitroimidazole antibiotics have been detected in the ecological environment of urban water bodies, with the content reaching 0.1–90.2 ng L^{-1} and the concentration in hospital wastewater even reaching 3.8 mg L^{-1} [6–8]. Thus, an efficient technology applied in MNZ removal is worth to be explored.

At present, various methods have been used in MNZ treatment, mainly including adsorption and advanced oxidation processes (AOPs) (e.g., electro-Fenton, photocatalytic degradation, and dielectric barrier discharge plasma (DBDP), etc.) [1,9–11]. Comparatively, DBDP is superior in rapidly decomposing contaminants by simultaneously producing a variety of active species, including O_3, H_2O_2, $^1O_2$, $O_2^{\bullet-}$, and $^{\bullet}OH$, etc. [12]. Compared to conventional energy consumption AOPs (e.g., Microwave, photocatalysis, and electro-catalysis), DBDP with under-current and various active species bring lower power required and faster treatment time [13–17]. Although solo-DBDP has become a highly efficient treatment technology, energy and treatment efficiency still have elevated space via the full use of active substances. Heterogeneous catalysis has been widely studied and applied in AOPs, also

---

including DBDP [18–20]. However, problems still exist, such as high ion dissolution, unstable catalysts, large dosage amounts, and difficult separation recovery. Thus, it is still a research topic to develop a stable and catalytic material compatible with DBDP.

The composite metal catalyst points to various metals or metal oxides by chemical bonds to form metal compounds, which have more surface-active sites via different valence states of transition metals and synergies between different metal redox. Mullite is a general term for a series of minerals composed of silica-aluminate. The general structure of mullite is AB_2O_5, where A is generally Bi, Y, Sr, or lanthanide elements, and B is generally Mn, Fe, and other transition metal elements [21,22]. $Bi_2Mn_4O_{10}$ has more excellent catalytic characteristics due to the Mn species in the lattice having two chemical states. The MnO_6 octahedra are intercalated by a Bi^{3+} or an Mn^{3+} plane along the c-axis, an admixture of direct interaction of Mn^{4+}–O–Mn^{4+} and an indirect interaction of Mn^{4+}–O–Mn^{3+}–O–Mn^{4+} a ferromagnetic coupling between Mn^{4+}, which form a deformed octahedral structure [23,24]. In mullite structure, the element Mn has different valence states and systems, increasing the surface oxygen vacancies [25]. Surface vacancies conducive to various catalysis, including hydrogen production [26], photocatalytic reforming of methanol [27], and organic pollutants degradation [28]. Previous researchers have studied the $Bi_2Mn_4O_{10}$ application in catalysis [29,30]. However, the application potential of $Bi_2Mn_4O_{10}$ in various AOPs, such as Fenton-like and catalytic O_3 oxidation, still needs to be investigated.

Herein, this study aims to elevate the performance of DBDP via the help of Nickel foam loaded with $Bi_2Mn_4O_{10}$ ($Bi_2Mn_4O_{10}$/NiF, BMON), which was synthesized by the assistant by microwave. The main objective could be summarized as i) NiF was used to increase the stability and recovery of $Bi_2Mn_4O_{10}$ and adjust the oxygen vacancy on the catalyst surface; ii) evaluate the antibiotics removal ability of the DBDP and DBDP/BMON systems based on MNZ degradation efficiency; iii) systematically analyzed the redox mechanism of the DBDP/BMON system and the microscopic effect in BMON; iv) propose the possible attacked-sites on MNZ, based on the combination of density functional theory (DFT) calculation and ESI-QTOF-MS detection. Finally, strengthening the applicability of the non-thermal plasma technology through the results, helping to form a promising technology for antibiotic removal.

2. Experiment

2.1. Materials

100 mm × 100 mm × 1 mm Nickel foam (NiF) was purchased from Christie's Foam Metal Co. Ltd (Suzhou, China). Bismuth nitrate (Bi (NO$_3$)$_3$·5 H$_2$O), manganese sulfate (MnSO$_4$·H$_2$O), nitric acid (HNO$_3$), hydrochloric acid (HCl), acetone (C$_3$H$_6$O), isopropanol (C$_3$H$_8$O), silver nitrate (AgNO$_3$), sodium hydroxide (NaOH), and potassium dihydrogen phosphate (KH$_2$PO$_4$) and dipotassium hydrogen phosphate (Na$_2$H-PO$_4$•7 H$_2$O) were brought from Sinopharm Chemical Reagent Co. (Shanghai, China). 5,5-Dimethyl-1-pyrroline N-oxide (DMPO), 4-Amino-2,2,6,6-tetramethylpiperidine (TEMP), metronidazole (MNZ), furfuryl alcohol (FFA), titanium potassium oxalate (C$_2$KO$_4$Ti), sodium indigo disulfate (C$_{16}$H$_8$N$_2$Na$_2$O$_8$S$_2$) and humic acid (HA, the main component is fulvic acid (FA), FA ≥ 90%), were brought from Aladdin Reagent Co. (Shanghai, China). All reagents used were of analytical grade without additional treatment, and the water was deionized (DI).

2.2. Synthesis of $Bi_2Mn_4O_{10}$/NiF

Pretreatment of NiF: the NiF purchased was cut into a sheet of 10 × 10 mm (thickness is 1.0 mm), and subsequent immersion in acetone for sonication was maintained for 20 min. Then, rinsed with DI water and placed in 6 mmol L^{-1} hydrochloric acids for 20 min. At last, rinsed with deionized water again until flushed clean and placed in a

vacuum oven for evaporating moisture.

Microwave-assisted coprecipitation method was used to synthesize $Bi_2Mn_4O_{10}$/NiF (BMON). First, dissolved 4.0 mmol MnSO$_4$·H$_2$O and 1.0 mmol Bi(NO$_3$)$_3$•5 H$_2$O into 20 mL HNO$_3$ solution (2 mol L^{-1}). After magnetic stirring for 30 min, a homogeneous mixed solution was obtained. Then immerse the pretreated NiF into the mixed solution and dropwise 100 mL NaOH solution (1 mol L^{-1}) under magnetic stirring until mixed evenly. Finally, transfer the mixture to a microwave reactor (COOLPEX-E, Preekem Scientific Instruments Co., Ltd., China)), set the microwave power at 150 W, and the microwave reactor started for 25 min. When the reaction solution was cooled to room temperature, separation of NiF from the liquid for being dried in a 70 °C oven. The sample was placed into a tube furnace and calcined at 600 °C for 2 h to obtain the BMON catalyst. $Bi_2Mn_4O_{10}$ is synthesized similarly to BMON, just without adding NiF.

2.3. Characterization of BMON

The morphological characteristics of the materials were characterized by an X-ray diffractometer (RD, D8 Advance, Bruker) and a scanning electron microscope with elements analysis by Energy Dispersive Spectroscopy (SEM&EDS, Sigma500, Zeiss) under additional magnification. X-ray photoelectron spectroscopy (XPS, ESCALAB 250Xi, Thermo Fisher) provided the chemical information and elements states. The crystal lattice was observed by Transmission electron microscope (TEM, JEM-2100, JOEL). The electron spin resonance spectrometer (ESR, ESP-300E, Bruker) detected oxygen vacancies on the material's surface.

2.4. Experimental procedures

The experimental device was designed as a coaxial cylindrical structure used for the experiment (Fig. S1). The detailed experimental procedures are as follows: i) Inject 200 mL of 10 mg L^{-1} MNZ-containing simulated wastewater into the reaction zone while turning on the water and air pumps. ii) Immerse the catalyst in the solution in the reaction zone, waiting for the discharge area and the reaction zone to complete the gas-liquid circulation; iii) Time counting starts immediately when the voltage is adjusted to be stable, and the solution is analyzed every 5 min for a specified time interval without stopping the discharge. iv) Turn off the power supply, and a complete experiment is finished. Particularly, the $Bi_2Mn_4O_{10}$ powder flows with the treated water, while BMON is a flake catalyst, which is not easy to run off and can be easily recovered from the aqueous. In addition, the cycling experiment was conducted by extended service time; every 30 min, replace 200 mL of 10 mg L^{-1} MNZ-containing aqueous. No additional treatment was done to the BMON.

2.5. Analytical methods

The samples collected in the experiment were detected with a UV−vis spectrophotometer (T6 new century, Pgeneral) to monitor the MNZ concentration. A 3 mL sample in a cuvette was measured at 318 nm. In addition, the HPLC equipment (LC-10A, Shimadzu) with a C18-P column (5 μm, 4.6 ×150 mm) and an ultraviolet detector with a detection wavelength of 277 nm was used to verify the accuracy of the UV−vis spectrophotometer. The concentration was calculated using the standard curve (Fig. S2). Based on the UV−vis detection, MNZ removal efficiency (ξ) was calculated as Eq. (1):

$$\xi(\%) = \frac{[MNZ]_0 - [MNZ]_t}{[MNZ]_0} \times 100\% \tag{1}$$

where $[MNZ]_0$ and $[MNZ]_t$ is the MNZ concentrations (mg L^{-1}) before and after discharge treatment, respectively.

During the discharge procedure, an oscilloscope, a high-voltage

probe, a low-voltage probe, and a 100 Ω resistor are used to detect the voltage value and calculate discharge power by the Q-V Lissajous graph method. The energy efficiency Y was calculated by Eq. (2):

$$Y(g\ kWh^{-1}) = \frac{[MNZ]_0 \times V \times \xi}{P \times t \times 1000} \tag{2}$$

where V is the reaction volume (L), ξ is the MNZ removal efficiency (%), P is the discharge power (kW), t is the discharge time and $[MNZ]_0$ is the initial MNZ concentration (mg L^{-1}).

H$_2$O$_2$ concentration was detected by the potassium titanate method [31,32], and sodium indigo disulfate was used to quantify the O$_3$ concentration [33]. The corresponding work curve is displayed in Fig. S3. DMPO and TEMP were used in radicals' detection by electron spin resonance spectroscopy (EPR, A300E, Bruker).

2.6. DFT calculation method

In this paper, based on the density functional theory (DFT), the active sites and possible bond-breaking positions of MNZ molecules were analyzed by calculating the Fukui function and Mulliken population.

The Fukui function expresses the Probability of electrophilic, nucleophilic, or free radical attack and estimates the active site of the molecule. Fukui functions can be divided into electrophilic and radical attacks ($f^{(-)}$ and $f^{(0)}$). The experiments were performed using the CASTEP module, which was used for Mulliken population analysis. In contrast, the DMol3 module was used in this study to calculate the Fukui index for the study.

3. Results and discussion

3.1. Characterization of BMON synthesized by microwave-assisted coprecipitation method

The XRD pattern in Fig. 1a depicted the crystallinity information of pure Bi$_2$Mn$_4$O$_{10}$ and BMON. A diffraction peak characterized fresh Bi$_2$Mn$_4$O$_{10}$ at a 2-Theta of 15.5°, 24.1°, 28.7°, 30.3°, 40.9°, and 58.6°, which were attributed to the (001), (120), (121), (211), (212), and (332) diffraction plane (Bi$_2$Mn$_4$O$_{10}$: JCPDS# 27–0048). Based on the Bi$_2$Mn$_4$O$_{10}$ orthorhombic space group (Pbam, #55), the cell parameters are a = 7.540 Å, b = 8.534 Å, and c = 5.766 Å. The XRD pattern qualitative the prepared Bi$_2$Mn$_4$O$_{10}$ was an orthorhombic space group of the
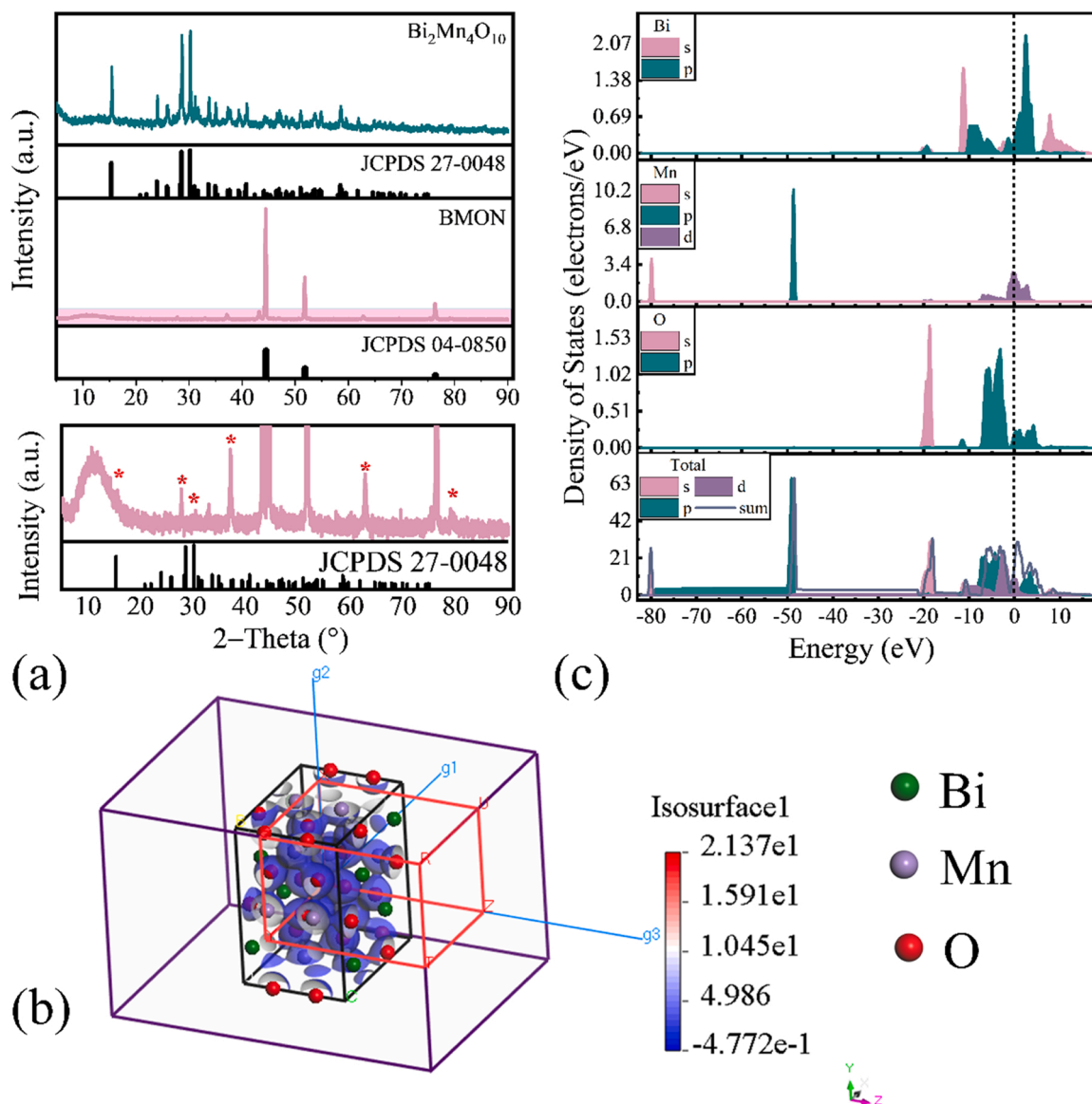

Fig. 1. XRD patterns (a) Charge densities (b) and density of states in different atomic orbitals of Bi$_2$Mn$_4$O$_{10}$ (c) (Brillouin zone of ORC lattice. Path: C–X–S–Y–C–Z–U–R–T–Z|Y–T|U–X|S–R).

mullite-type and had the application stability. The diffraction peaks appear at 44.51°, 51.85°, and 76.37°, corresponding to (111), (200), and (220) lattice plane defined by miller indices, respectively. Due to the strong signal of cubic crystal nickel (Ni: JCPDS# 04–0850), typical $Bi_2Mn_4O_{10}$ diffraction peaks are covered. After enlarging the low-intensity peaks, a sharp peak-shaped BMON diffraction was observed. The XRD pattern indicated that $Bi_2Mn_4O_{10}$ was successfully crystallized on the NiF surface. Based on the XRD diffraction results (Pbam #55 space group) the CASTEP module is used to calculate the charge densities and partial density of states of $Bi_2Mn_4O_{10}$ [34]. Due to the electronegativity, electrons around Bi are easily mobile and the electron cloud is mainly concentrated around Mn and O (Fig. 1b). As shown in the partial density of states (PDOS) image (Fig. 1c), the left side of the Fermi energy level is the valence band, mainly composed of s and p orbitals, with some contribution from d orbitals; the right side of the Fermi energy level is the conduction band, consisting primarily of p and d orbitals. Based on the density of states analysis results, speculating that mainly s and p orbitals are involved in bonding, and the free electrons are primarily distributed in p and d orbitals.

SEM and TEM characterized the morphology and size of the synthesized $Bi_2Mn_4O_{10}$. As shown in Fig. S4, the prepared powder $Bi_2Mn_4O_{10}$ presents small particles in the shape of spheroids or rice grains, and most of them are agglomerated distribution in the form of starfish or lotus with a diameter of 20 μm. To observe the lattice structure, continue to magnify $Bi_2Mn_4O_{10}$ by TEM, and the result is shown in Fig. 2a and b. The $Bi_2Mn_4O_{10}$ nanoparticles consist of dense sticks ranging from tens to hundreds of nanometers. In addition, typical crystal planes of $Bi_2Mn_4O_{10}$ were observed by the high-resolution transmission electron microscope (HRTEM). The lattice spacing of 0.31 nm, 0.58 nm,

and 0.29 nm is consistent with the (0 0 1), (1 2 1), and (2 1 1) crystal planes of orthorhombic phase $Bi_2Mn_4O_{10}$ [35,36]. As shown in Fig. 2c, the NiF is a smooth metal mesh with a skeleton width of around 50 μm. Because of the lotus-shaped $Bi_2Mn_4O_{10}$ attached to the NiF skeleton, The surface of BMON is rougher (Fig. 2d and e), indicating that the close-fitting occurs between $Bi_2Mn_4O_{10}$ and NiF. Due to Ni participating in catalyst synthesis, compared with the enlarged $Bi_2Mn_4O_{10}$ particles (Fig. S4c and d), the crystal flower, stacked by short nanorods, on the BMON amplificated has a smoother structure (Fig. 2f). The elements' distribution and content are displayed in Fig. 2j–k. The O, Mn, and Bi atomic ratio is about 8:2:1, concentrated on crystalline flowers. The carrier Ni is involved in the formation of the surface catalyst, causing Ni to be observed simultaneously in the carrier skeleton and crystallization position, which is consistent with the results observed by SEM. The investigation of morphology, microstructure, and lattice structure of $Bi_2Mn_4O_{10}$ and BMON found that ternary catalyst solidified onto flakes was successfully synthesized.

The XPS image, presented in Fig. S5, has inspected the chemical states of the as-prepared $Bi_2Mn_4O_{10}$. According to the XPS survey in Fig. S5a, the $Bi_2Mn_4O_{10}$ is composited by Mn, O, and Bi elements. The high-resolution spectra of Mn 2p is the asymmetrical peaks decomposed by curve fitting. As shown in Fig. S5b, the deconvolution peak divided into 643.0 eV and 642.1 eV were attributed to the surface Mn^{4+} and Mn^{3+} [30,37]. As investigated, the recycling between $Mn^{4+}\leftrightarrow Mn^{3+}$ is associated with the activity sites of the Mn-based catalyst, which suggests the catalytic potential of the $Bi_2Mn_4O_{10}$ [38]. The peaks at binding energies of 164. 4 eV and 159. 1 eV are attributed to Bi 4 $f_{2/5}$ and Bi 4 $f_{7/2}$ in Fig. S5c, illustrating that Bi^{3+} was a part of $Bi_2Mn_4O_{10}$ [39]. The oxygen species can be discriminated by O 1 s XPS spectra, as shown in
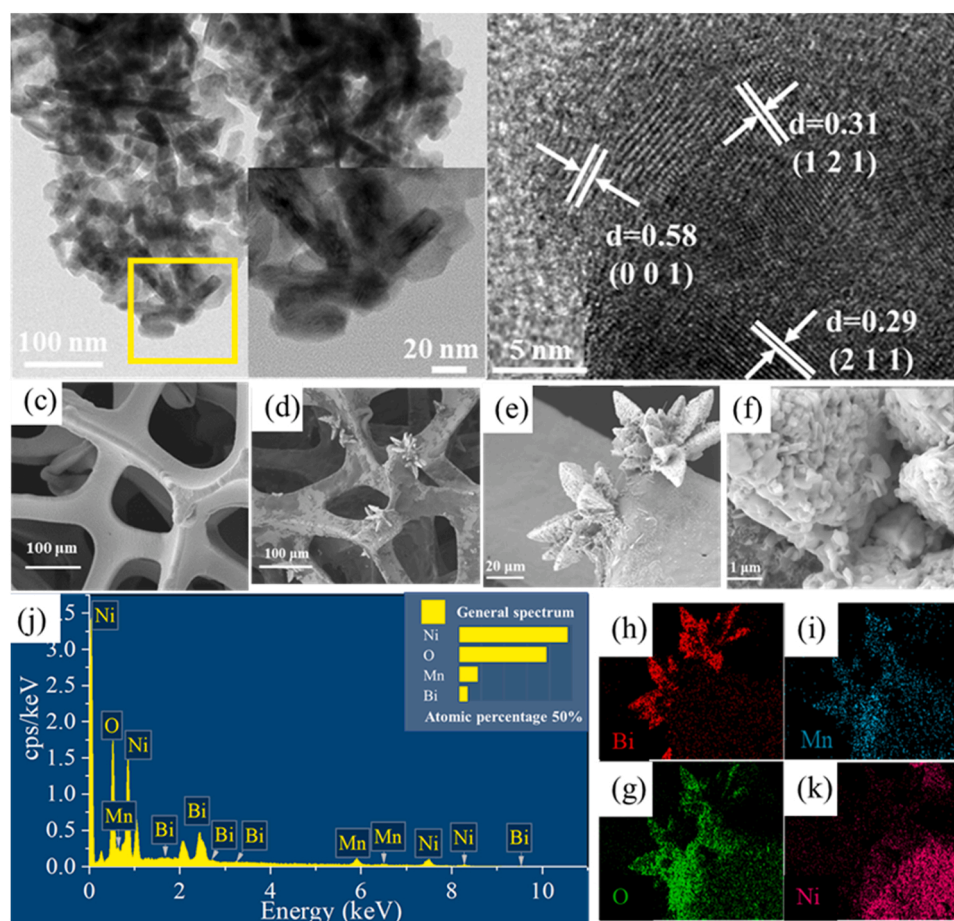

Fig. 2. TEM (a) and HRTEM (b) of $Bi_2Mn_4O_{10}$; SEM image of NiF (c), BMON (d-f); BMON EMSA/MAS spectral (j); Bi (h), Mn (i), O (g), and Ni (k) of BMON EDS spectrum.

Fig. S5d. The deconvoluted peaks of surface hydroxide (-OH), lattices oxygen (O^{2-}, defined as O_L) center at 532.5 eV and 531.4 eV; the surface adsorbed oxygen (O_2^{2-}, defined as O_A) appeared at 529.8 eV, which is derived from dissociative oxygen on oxygen vacancies ($V_ö$) [40–43]. The relative content of O_A ($Bi_2Mn_4O_{10}$ 17.41%, BMON 58.37%) is calculated and collected in Table S1. The presence of O_A was associated with $V_ö$ concentration and the ratio of Mn^{4+}/Mn^{3+} [44]. On account of the theory of electrostatic balance, the number of Mn^{3+} is used as a parameter to assess the concentration of the $V_ö$, and the formula is as shown in Eq. (3) [25].

$$-Mn^{4+}-O^{2-}-Mn^{4+}\rightarrow -Mn^{3+}-\square-Mn^{3+}-+\frac{1}{2}O_2 \qquad (3)$$
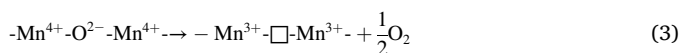
where $\square$ represents the formation of $V_ö$, the content of Mn^{3+} formation corresponds to the relative amount of $V_ö$. Therefore, the higher concentration of Mn^{3+} implies a higher concentration of $V_ö$, which has a vital function for the catalytic reaction. Based on the theoretical calculation and experimental verification, $V_ö$ could be the reactive site on the catalyst surface by changing the surface properties of electronics and chemicals [45]. ESR can detect the valuable fingerprinting information of unpaired electrons, and metal oxide with $V_ö$ might have unpaired electrons. As shown in Fig. 3, ESR spectra exhibited two intense symmetrical lines with the central g factor at 2.003, representing $V_ö$ [46]. With the addition of NiF, the content of Mn^{3+} and O_A increased by 22.1% and 13.7% in Table S1, and the increasing ESR signal intensities demonstrate a similar result with XPS that Ni dope promotes the increase of $V_ö$ content. According to the neutrality principle, the formation of $V_ö$ by doping elements with lower oxidation states compared to the host ions. An increase of $V_ö$ in metal oxides could be achieved by doping lower cations oxidation states. Research in other references found that based on the neutrality principle, doping lower oxidation states elements than host ions encourages the formation of $V_ö$ [47]. Both XPS and ESR detection suggest the effect of NiF on Vö generation promotion.

3.2. MNZ removal in different reaction systems

The discharge effect produces various active species, including O_3, H_2O_2, $^1O_2$, $^•OH$, and $O_2^{•-}$. Meanwhile, these substances are generated and transformed through a gas-liquid surface to attack the target contaminants. As shown in Fig. 4a, the solo-DBDP could remove 66.8% MNZ within 25 min, which still has space for improvement by increasing the utilization of the active substances. The contaminants removal capacity was significantly improved by the introduced catalyst $Bi_2Mn_4O_{10}$, and the corresponding MNZ removal increased to 97.9%. However, although the degradation capacity was enhanced, the addition of the catalyst brought the problem of metal ion leaching. 1.946 mg L^{-1} Mn has been close to the standard limit of 2 mg L^{-1} (GB 18918–2002, China) in Fig. 4b. Immobilization of the powder $Bi_2Mn_4O_{10}$ on NiF reduces the dissolution of Bi and Mn during the water treatment process, also

maintained a stable catalytic capacity. The dissolved amount of Bi and Mn decreased from 7 µg L^{-1} and 1.964 mg L^{-1} to 2 µg L^{-1} and 0.232 mg L^{-1} respectively, and the MNZ removal rate in DBDP/BMON was elevated to 0.1690 min^{-1}, which was faster than 0.04798 min^{-1} and 0.1318 min^{-1} of solo-DBDP and DBDP/$Bi_2Mn_4O_{10}$ system.

A high input voltage can produce more significant physicochemical effects, more active substances, and higher energy consumption. Thus, a suitable discharge voltage is essential in DBDP/BMON synergistic process, and the investigation results are displayed in Fig. 4c and d. When elevated the input voltage, the MNZ removal efficiency increased in both the DBDP and the DBDP/BMON. The most noticeable improvement was obtained (from 49.3% to 75.3%) with the highest energy utilization increases of 0.3474 g kWh^{-1} at 16 kV, illustrating that the addition of BMON enhances the MNZ removal ability of the DBDP process. Nevertheless, a higher energy utilization appeared at 18 kV (1.142 g kWh^{-1}), the MNZ degradation efficiency was promoted to 99.4%, and the removal rate was 3.12 times that at 16 kV. To reveal the interrelationship of input voltage and MNZ removal, the oxidants yield under the input voltage from 12 kV to 20 kV were depicted in Fig. S6. The concentration of O_3 and H_2O_2 gradually increased with the input voltage from 12 kV to 18 kV, and then O_3 concentration continues increasing but H_2O_2 content decreased at 20 kV. Discharge electrons would be accelerated by a stronger electric field, higher velocities leading to more intensive particle collisions, and more active species were generated. The process of aeration supplements oxygen to the reactor, and the gas flow through the discharge area continuously generate O_3. However, excess O_3 reacts with H_2O_2, causing the concentration drop. The decrease would not inhibit the degradability of the system because H_2O_2 was converted into $^•OH$, which has a stronger oxidizing potential [48].

The solution circulation influences both residence time through the discharge region and mass transfer in the reaction area. As shown in Fig. 5a, the solution circulation effects the DBDP and DBDP/BMON similarly but is more evident in DBDP/BMON. Along with the circulation rate rising from 100 mL min^{-1} to 300 mL min^{-1}, the MNZ elimination tended to increase first and then decrease. The maximum value of 98.8% and 78.1% were achieved at 150 mL min^{-1} in DBDP and DBDP/BMON, respectively. Besides, in Fig. 5b, the corresponding k and Y are 0.07513 min^{-1} and 0.8473 g kWh^{-1} in DBDP, 0.1657 min^{-1} and 1.142 g kWh^{-1} in DBDP/BMON, illustrating that DBDP/BMON is a more efficient system in MNZ removal and energy utilization than DBDP. The rise of circulation rates could reduce the single-cycle residence time (effective residence time) between solution and discharge plasma, hindering the transformation of H_2O_2 to $^•OH$, but beneficial for mixing active substances with aqueous. Although the cycle numbers increased with the water circulation rate, the effective residence time in the discharge area contributes more to the degradation ability [49]. Thus, for efficient MNZ removal, there is an equilibrium point under positive and negative influences, which is the optimal cycle rate operating parameter, 150 mL min^{-1} in DBDP/BMON and DBDP.

3.3. Influence of experimental circumstance on MNZ removal

3.3.1. Optimization of operating parameters of DBDP/BMON process

For the DBDP/BMON process, it is necessary to figure out the limitations of the application scope. The appropriate BMON dosage and the applicable range of MNZ elimination concentration were investigated, and the results are displayed in Fig. 6. The MNZ removal was significantly improved by the BMON dosage increasing from 1/4, 1/2, to 1 piece. Nevertheless, a further increase to 2 pieces could not obtain a higher removal efficiency, which means that the catalyst dosage had reached saturation (Fig. 6a). Fig. 6b also shows that excessive catalyst dosing could not get an additional increase in energy utilization and degradation rate. Therefore, considering the excess catalysts ineffectively utilized, 1 piece of BMON is the best choice for the treatment conditions. There is a concentration range that DBDP/BMON process
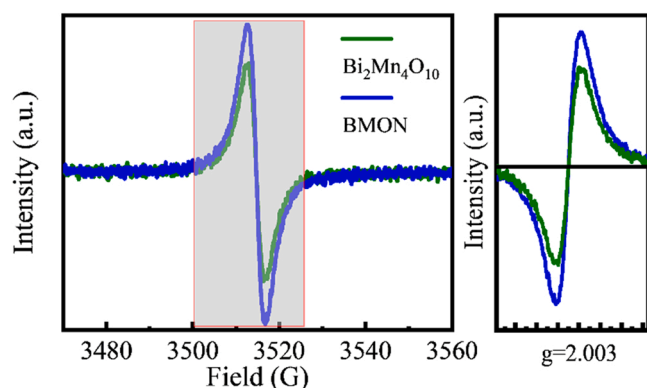

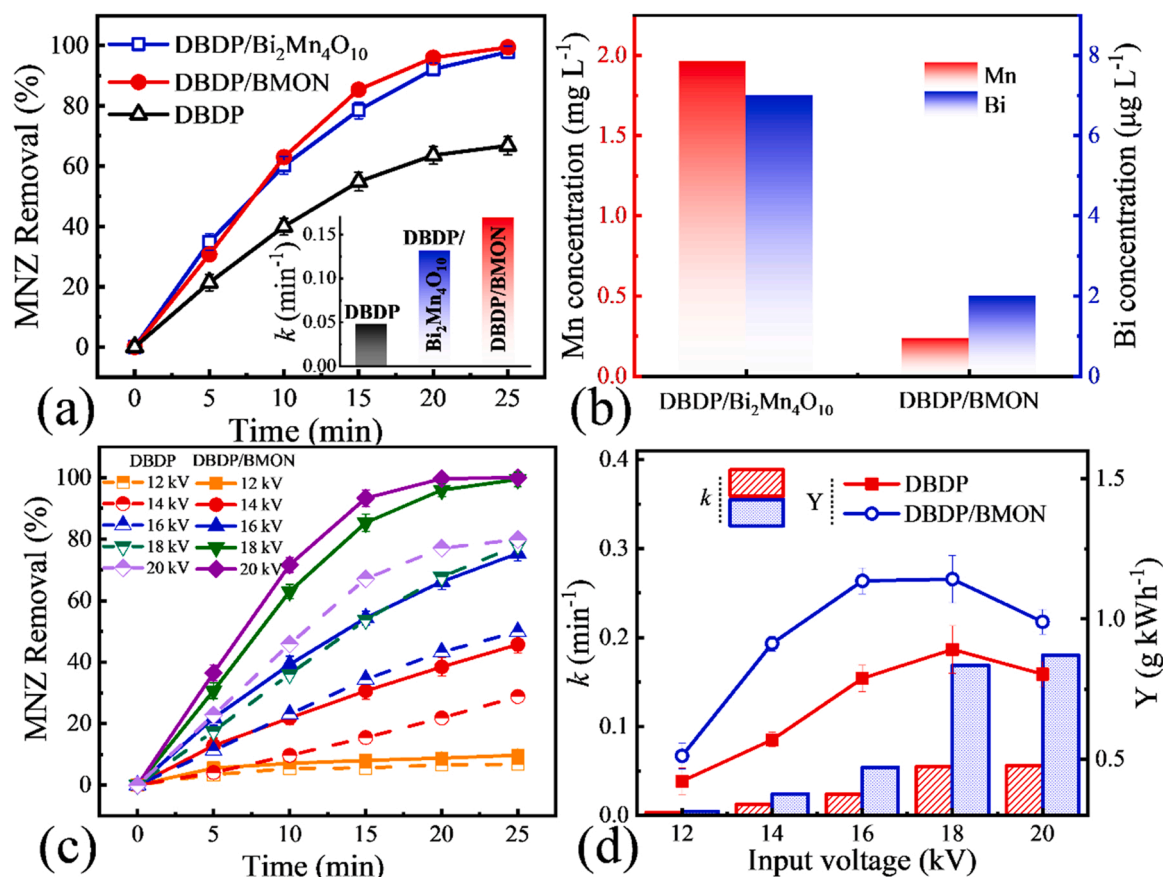**Fig. 3.** EPR spectra of BMON and $Bi_2Mn_4O_{10}$.

Fig. 4. MNZ removal in different DBDP system (a) and ion concentration after degradation (b) Input voltage influence on MNZ removal (c), removal rate, and energy efficiency (d), in DBDP and DBDP/BMON system. Input voltage influence on H_2O_2 and O_3 yield in DBDP (e). Reaction condition: V= 200 mL, [MNZ]= 10 mg L^{-1}, catalyst dosage= 1 piece, water circulation rate= 150 mL min^{-1}.
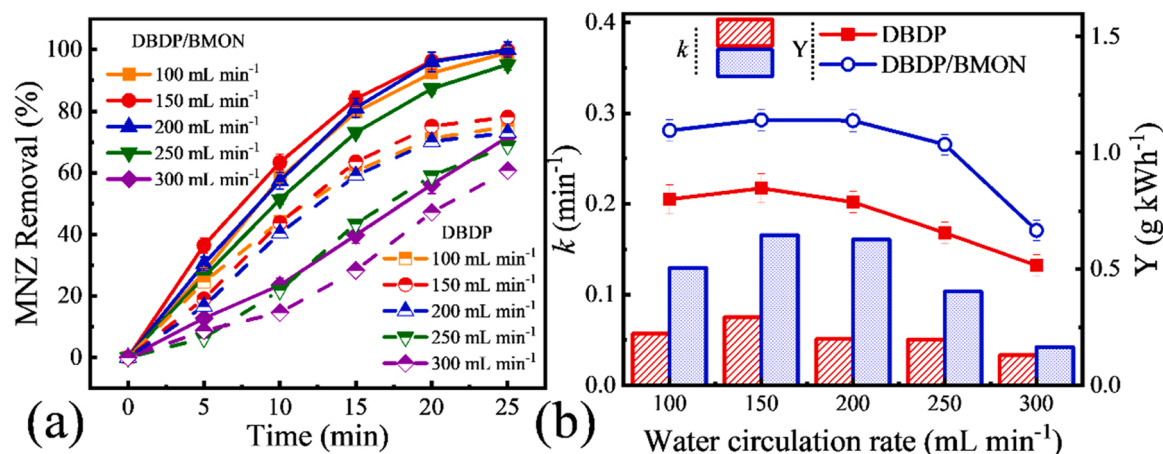

Fig. 5. Flow rate effect on MNZ removal (a), removal rate, and energy efficiency in DBDP/BMON system (b). Reaction condition: V= 200 mL, [MNZ]= 10 mg L^{-1}, catalyst dosage= 1 piece, water circulation rate= 150 mL min^{-1}.

can handle MNZ in a limited-time. As Fig. 6c proposed, almost 100% of MNZ could be removed by DBDP/BMON when the MNZ concentration is below 10 mg L^{-1}. To clearly analyze the MNZ concentration influences, data were collected within 18 min, and the results are shown in Fig. 6d. Notably, although the removal efficiency of 5 mg L^{-1} was similar to that of 10 mg L^{-1} in the DBDP/BMON process, the removal rate was 1.5 times (0.180 min^{-1} to 0.118 min^{-1}). When determining the operating parameters of DBDP and BMON dosage, the content of active substances is simultaneously stable, and the degradation rate will inevitably slow

down as the target pollutant increases. A further addition above 10 mg L^{-1}, the removal rate decreased significantly. The reason might be that the excess pollutants consume the active substances continuously generated, and the concentration of active substances limits the degradation rate. Thus, the degradation rate might be determined by the generation rate of active substances in DBDP/BMON.

The initial aqueous pH impacts the molecular Ion formation of solute (active species and contaminants) and the catalyst in the heterogeneous system, which is directly associated with the catalytic performance.
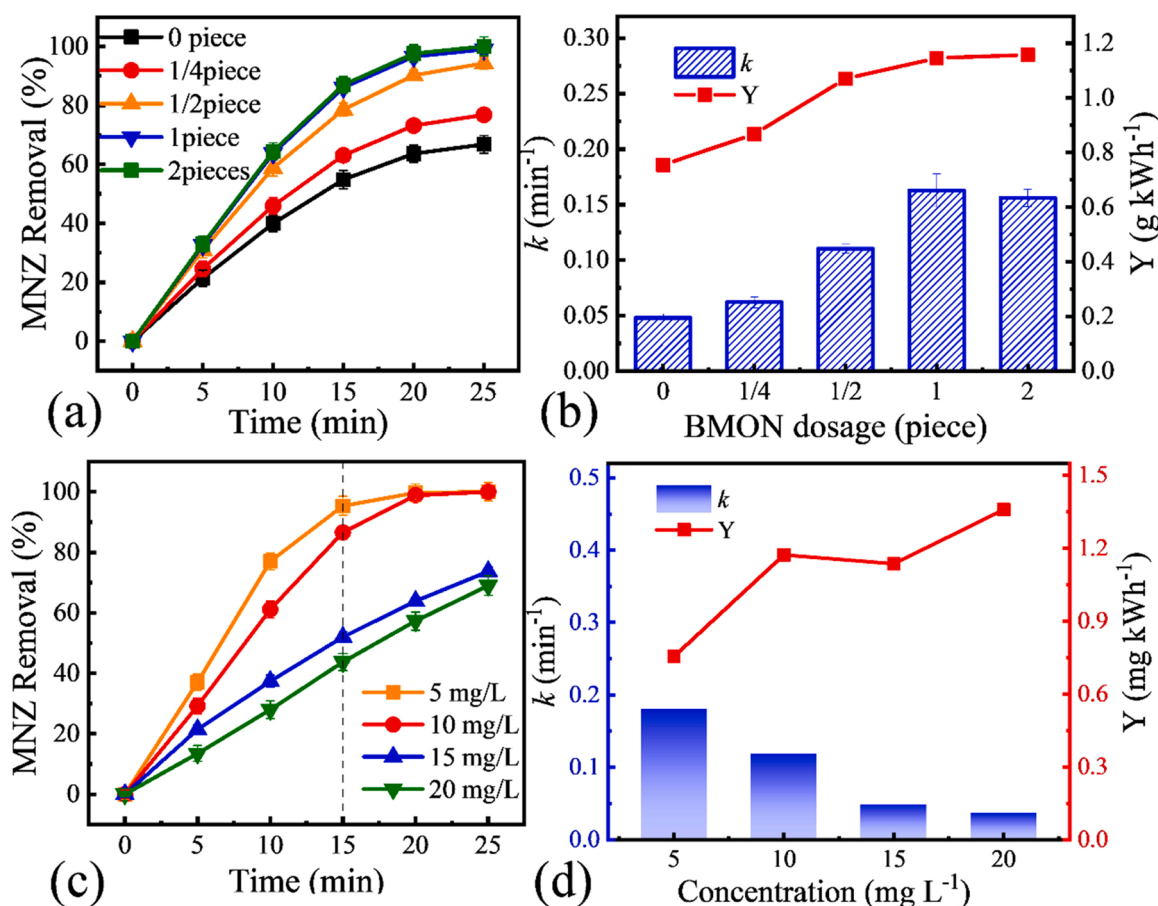
Fig. 6. Catalyst dosage effect on MNZ removal (a), removal rate, and energy efficiency in DBDP/BMON system (b). MNZ concentration effect on MNZ removal (c), removal rate, and energy efficiency in DBDP/BMON system (d) Reaction condition: V= 200 mL, [MNZ]= 10 mg L^{-1}, catalyst dosage= 1 piece, input voltage= 18 kV.

Thus, the pH effect of initial pH (pH= 2, 4, 6, 8, and 10) on MNZ degradation in the DBDP/BMON process, and the result is presented in Fig. 7a. Almost complete MNZ removal (97.10%~ 98.34%) was achieved at pH 6–10, with the k value of 0.1333, 0.1410 and 0.1468 min^{-1}; the energy efficiency was 1.080 g kWh^{-1},1.118 g kWh^{-1} and 1.128 kWh^{-1}, respectively in Fig. 7b. This phenomenon suggests the DBDP/ BMON process has a wide working pH range and includes the pH of natural water bodies. The DBDP/BMON process retains a relevant high MNZ removal (87.2%) and energy utilization (1.002 g kWh^{-1}) under weak acid conditions but could not work in a strong acid circumstance. The MNZ degradation tendencies due to pH changes are consistent with the work of Wang et al. [37]. As shown in Fig. 7c, at the end of the process, under the affection of small molecules of acid produced during the discharge and degradation, the system pH is close to 4. However, the products can't affect the over-acidic system, and before and after the reaction, the pH remained around 2. These phenomena could be summarized as the following reasons. First, the initial pH is below 3.03: i) when the pH is below the pKa of MNZ, causing MNZ mainly exists with a positive electric charge form (Fig. S7a), and electrostatic repulsion between MNZ hinders the degradation process; ii) Acidic environment can affect the stability of BMON structures. Secondly, the initial pH is from 3.03 to 6.20: When the initial pH is lower than the BMON surface zeta potential (Fig. 7d), the positively charged BMON tends to attract nitroimidazole structure with high electron cloud density and promote degradation. At last, the initial pH above 6.20: i) As shown in Eqs. (4) and (5), increasing pH benefits O$_3$ transform to •OH [50]; ii) An alkaline environment is more favorable for electrophilic reaction.

$$2H_2O_2 + 2O_3 \rightarrow H_2O + 3O_2 + HO_2^\bullet + \bullet OH \tag{4}$$
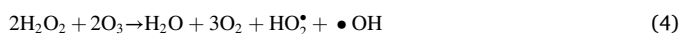
$$k_{obs} = k_{HO_2^-,O_3} \times 10^{(pH-pKa)} \tag{5}$$

where k_{obs} is the apparent second-order rate constant (M^{-1} s^{-1}), $k_{HO_2^-,O_3} = 9.6 \times 10^6$ M^{-1} s^{-1}, the pK_a of H$_2$O$_2$ is 11.8, and pH represent the pH of the solution.

3.3.2. The water matrix influence on the DBDP/BMON process in MNZ removal

Natural water bodies contain ubiquitous inorganic ions and other matter, leading to a complex water environment, affecting the radical-induced reactions in the AOPs process [51]. To evaluate the results of different inorganic anions on the catalytic MNZ degradation, and compare the effects of different ions, several inorganic salts with 1 mM, including NaCl, NaNO$_3$, Na$_2$CO$_3$, and Na$_2$SO$_4$, were deliberately spiked into the DBDP/BMON system. The effect of the same amounts of various anions on the MNZ degradation is shown in Fig. 8a, and the pH change induced by ion addition is also shown in Fig. S8a. Furthermore, to investigate the affection of each ion, the addition of different ion concentrations' effect results in degradation efficiency, and the rate is also shown in Figs. 8b–f and S8b–e detailed. The co-existing SO$_4^{2-}$ had negligible influence on MNZ removal by the DBDP/BMON process, and the hindrance order of the rest co-existing ions is CO$_3^{2-}$ > Cl$^-$ > NO$_3^-$. Based on the distribution of ion species, between pH 10–11, carbonate mainly exists in the form of HCO$_3^-$ and CO$_3^{2-}$ (Fig. S7b). Therefore, ion influence might be attributed to the reaction rate with •OH. Specifically, as shown in Eqs. (6)–(9), Cl$^-$ and CO$_3^{2-}$ have a higher reaction rate with •OH, but compared with CO$_3^{\bullet-}$, chlorine radicals with the redox potential in MNZ degradation [52], and under acidic conditions, •OH cannot oxidize SO$_4^{2-}$ to a stronger oxidant SO$_4^{\bullet-}$ [53].
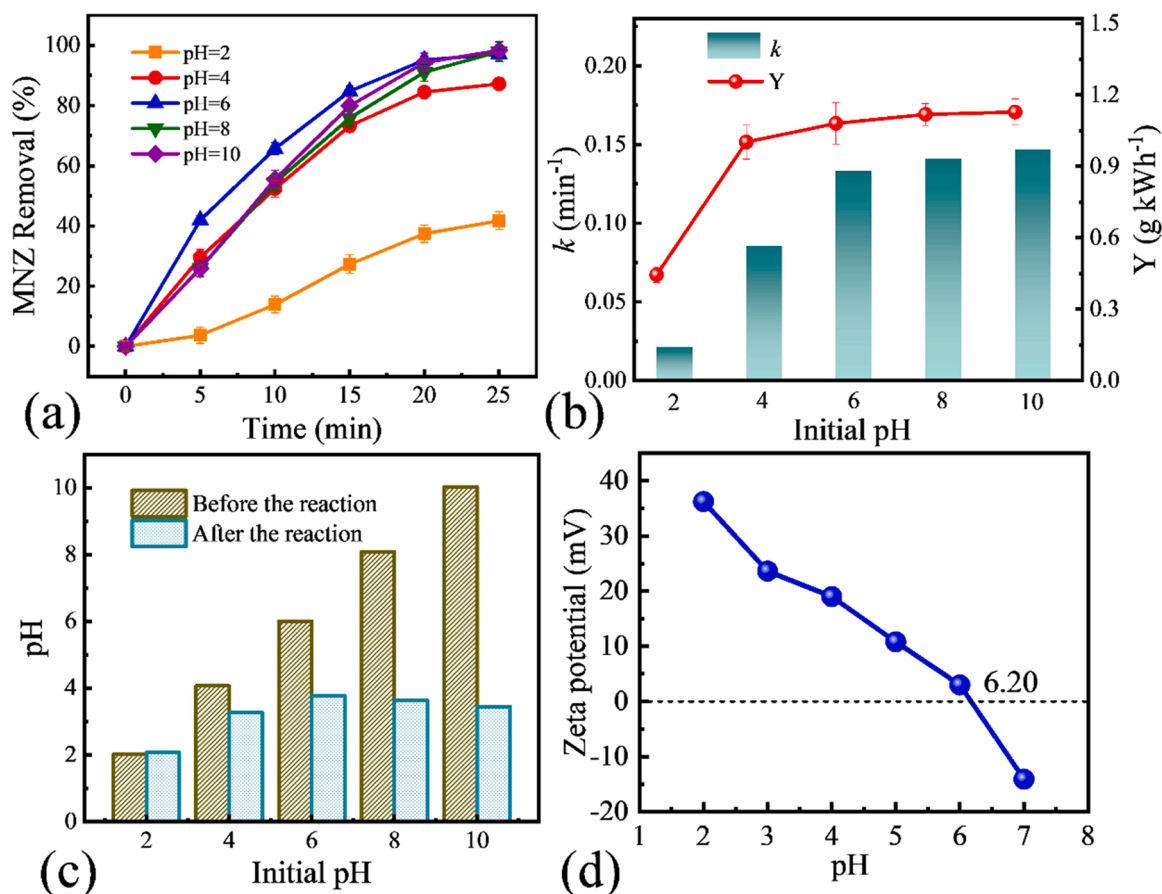
Fig. 7. Initial pH effect on MNZ removal (a), removal rate, and energy efficiency in DBDP/BMON system (b) pH change(c), and Zeta potential of BMON. Reaction condition: V= 200 mL, [MNZ]= 10 mg L^{-1}, water circulation rate= 150 mL min^{-1}, input voltage= 18 kV.

The influence of various SO_4^{2-} and NO_3^- concentration levels on the elimination of MNZ were studied and shown in Fig. 8c and d. With increasing the concentration of SO_4^{2-} and NO_3^- from 0.1 to 10 mM, the removal efficiency and the corresponding k of MNZ have no significant change. Specifically, less than 5% fluctuation in degradation termination and the difference between the pseudo-first-order rate constant is below 0.05 min^{-1}. This phenomenon could be explained by the fact that both SO_4^{2-} and NO_3^- are not powerful scavengers for active radicals. Ren et al. found a similar phenomenon in the DBD + CoOOH system [54], VUV/Fe^{2+}/H$_2$O$_2$ system by Wang et al. [52], and the ozone system by Qin et al. [55]. However, Zhu et al. found different results in their investigation, in which NO_3^- positively influences PFOA elimination [56]. The difference in research is mainly attributed to the difference in DBDP generator and operation parameters. In Zhu's study, the input voltage of a DBDP generator with a helical electrode reaches up to 21 kV, under which NO_3^- can be converted into ONOOH. This strong oxidizer can react directly with pollutants and produce •OH. The different results illustrate the potential of DBDP system research, DBDP generator structure development, and utilizing various active species have the investigation space.

Fig. 8e shows the MNZ degradation under the effect of different Cl$^-$ concentrations from 0.1 mM to 10 mM. Noteworthily, Cl$^-$ performed a dual impact on the DBDP/BMON system. With the addition of Cl$^-$ increase from 0 to 0.1 mM, the degradation efficiencies decreased from ~100–79.4%. However, with the Cl$^-$ concentration further increased, the removal of MNZ was increased to 90.4%. As expected, the k evolution tendency was consistent with the MNZ removal. Similar inhibitory and recoverability of Cl$^-$ in other AOPs processes were also reported, including Co$_3$O$_4$-Bi$_2$O$_3$/PMS process by Hu et al. [54] and Co^{2+}/oxone process by Wang et al. [57]. The influence of Cl$^-$ on the DBDP/BMON

system can be explained by Eqs. (9)–(12). Chlorides are an exceptional case of halogen elements because apart from their apparent action as scavengers (3–4.3 × 10^9 M^{-1} s^{-1} for •OH), they have been reported to enhance the degradation of organic pollutions by a series of chlorine-containing radicals generated from the reaction between •OH and Cl$^-$ [53,58]. When the Cl$^-$ dosage exceeds 0.1 mM, part of them was transformed to Cl•, HOCl•$^-$, and Cl$_2$•$^-$, which might benefit the DBDP/BMON process in MNZ removal. Therefore, the decline and gradual recovery phenomena were attributed to offsetting the inhibition and promotion effects.

Carbonate as an •OH scavenger and strong base and weak acid salt could significantly affect both radical reaction and solution pH environment. Its effect on MNZ removal in the DBDP/BMON process was explored. As shown in Eqs. (13 and 14), the addition of carbonate could proceed to hydrolysis with H$_2$O, and the released OH$^-$ raising the solution pH to an alkaline environment, which was beneficial for MNZ degradation. In addition, the buffering effect of CO$_3^{2-}$ led to the change in the active species and quantity in the DBDP/BMON process. Therefore, adding a small amount of carbonate would promote MNZ degradation. When the CO$_3^{2-}$ concentration was increased from 0 to 0.1 mM, the removal rate slightly increased from 0.1380 min^{-1} to 0.1676 min^{-1}. Weak stimulatory effects could be attributed to the changes in pH value. However, a further increase would only result in a continuous decrease in the degradation rate. The inhibition degree deepened with the increase of CO$_3^{2-}$ concentration and the k corresponding to 1 mM, 5 mM, and 10 mM carbonate concentration were 0.0995 min^{-1}, 0.0312 min^{-1}, and 0.0245 min^{-1}. Excess CO$_3^-$ and HCO$_3^-$ are potent scavengers of •OH, but the generation CO$_3$•$^-$ is a weakened radical [39,59]. Therefore, the impaired MNZ removal efficiency in DBDP/BMON process was ascribed to the lower redox capacity of carbonate radicals and the reduction of
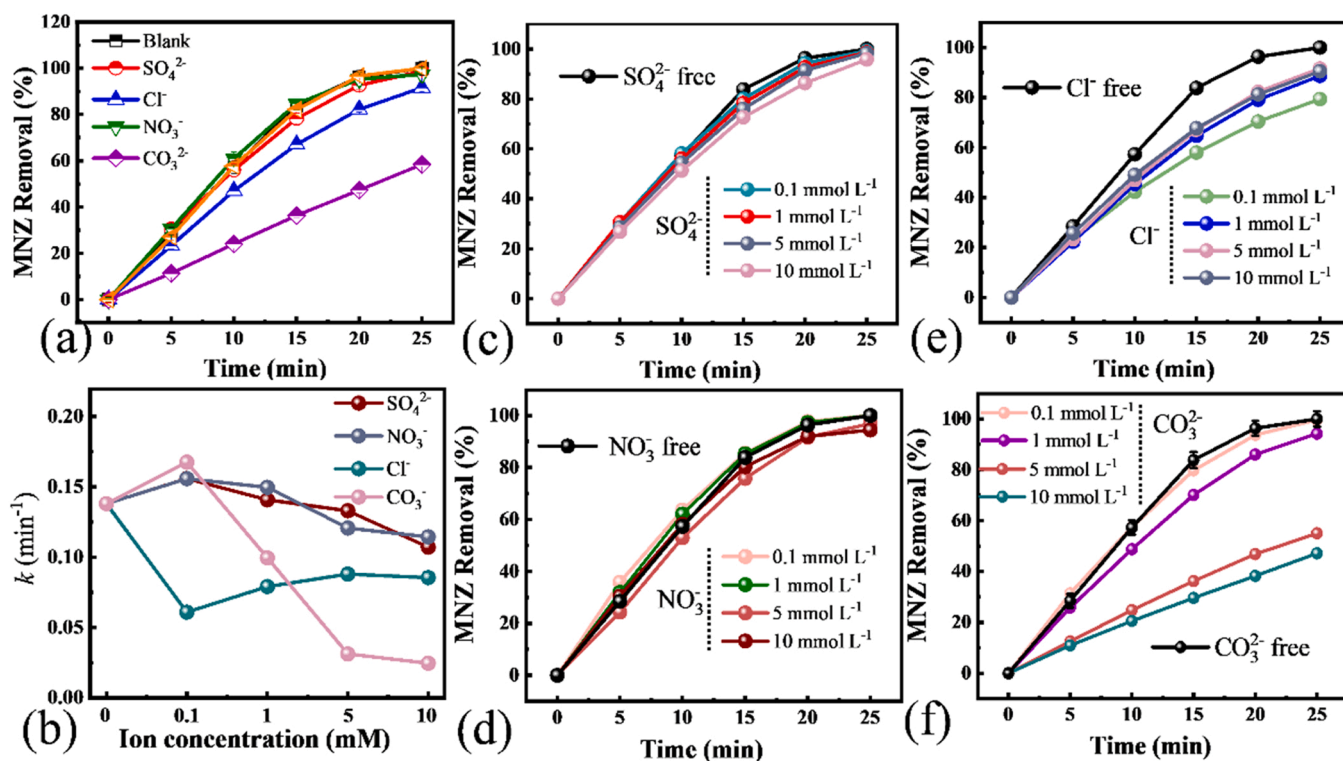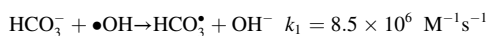
Fig. 8. Co-existing ion effect on MNZ removal (a), and removal rate changes (b). Different concentration of SO_4^{2-} (c), NO_3^- (d), Cl^- (e), and CO_3^{2-}(f) effect on MNZ removal in DBDP/BMON system. Reaction condition: V= 200 mL, [MNZ]= 10 mg L^{-1}, water circulation rate= 150 mL min^{-1}, input voltage= 18 kV.

•OH amount.

$$HCO_3^- + •OH \rightarrow HCO_3^• + OH^- \quad k_1 = 8.5 \times 10^6 \ M^{-1}s^{-1} \quad (6)$$

$$CO_3^{2-} + •OH \rightarrow + CO_3^{•-} + OH^- \quad k_2 = 4 \times 10^8 \ M^{-1}s^{-1} \quad (7)$$

$$NO_3^- + •OH \rightarrow NO_3^• + OH^- \quad k_3 = 5.0 \times 10^5 \ M^{-1}s^{-1} \quad (8)$$

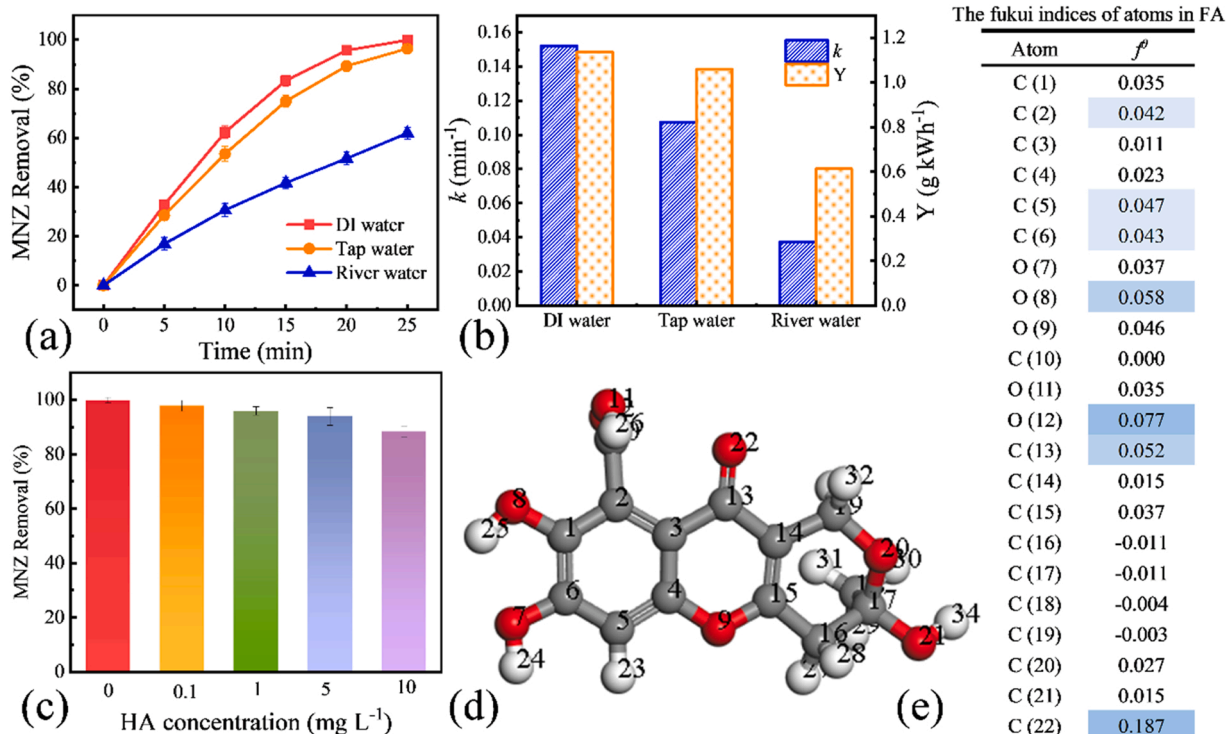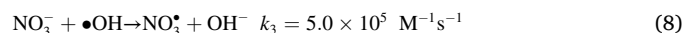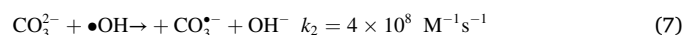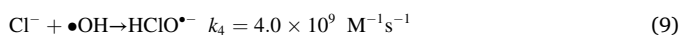| The fukui indices of atoms in FA	
Atom	f^0
C (1)	0.035
C (2)	0.042
C (3)	0.011
C (4)	0.023
C (5)	0.047
C (6)	0.043
O (7)	0.037
O (8)	0.058
O (9)	0.046
C (10)	0.000
O (11)	0.035
O (12)	0.077
C (13)	0.052
C (14)	0.015
C (15)	0.037
C (16)	-0.011
C (17)	-0.011
C (18)	-0.004
C (19)	-0.003
C (20)	0.027
C (21)	0.015
C (22)	0.187

Fig. 9. Different water matrix effect on MNZ removal (a), removal rate, and energy efficiency (b), and HA effect on MNZ removal (c) in DBDP/BMON system. The Fukui indices of atoms in FA (d) and (e). Reaction condition: V= 200 mL, [MNZ]= 10 mg L^{-1}, water circulation rate= 150 mL min^{-1}, input voltage= 18 kV.

$$Cl^- + \bullet OH \rightarrow HClO^{\bullet-} \quad k_4 = 4.0 \times 10^9 \text{ M}^{-1}\text{s}^{-1} \tag{9}$$

$$HClO^{\bullet-} + H^+ \leftrightarrow Cl \bullet + H_2O \tag{10}$$

$$Cl \bullet + Cl^- \rightarrow Cl_2^{\bullet-} \tag{11}$$

$$Cl_2^{\bullet-} + H_2O \leftrightarrow HClO^{\bullet-} + H^+ + Cl^- \tag{12}$$

$$H_2CO_3 \rightleftharpoons H^+ + HCO_3^-, \quad pK_{a1} = 6.38 \tag{13}$$

$$HCO_3^- \rightleftharpoons H^+ + CO_3^{2-}, \quad pK_{a1} = 10.38 \tag{14}$$

To evaluate the practical potential of the DBDP/BMON process, various water matrices, including DI water, tap water, and river water (Songhua River, China), whose characteristics are shown in Table S2, were introduced to examine the system's oxidative ability. As shown in Fig. 9a and b, approximately 100% of MNZ was removed in DI and tap water, but only 61.7% of MNZ was removed in the river water. The corresponding energy utilization and k decreased to 0.6126 g kWh^{-1} and 0.0374 min^{-1}, respectively. Different from DI water and tap water, the high TOC content and Cl$^-$ concentration in river water might be the reason that hinders MNZ degradation. As shown in Fig. 9c, with the increase in the concentration of natural organic matter (HA), the degradation efficiency of MNZ gradually decreased. Similar results appeared in other systems including CuO-Fe$_2$O$_3$/MXene + PMS by Xu et al. [59] and MW + PS + Fe$_3$O$_4$ by Hu et al. [60]. Fig. 9d and e display the DFT calculation results of FA (the major component of NOM), the

higher Fukui indices of FA illustrating that radicals are more likely to destroy the hydroxyl oxygen and carbonyl oxygen of FA than MNZ. Therefore, other organic matter and ions could explain this hindrance phenomena in the river water, which could hinder partial MNZ elimination and competition with target contaminants for active species.

3.3.3. The stability of the DBDP/BMON system

Reusability is a critical parameter of the DBDP/BMON system for the catalyst's cost-effective application in wastewater treatment. BMON was further tested for recovery catalysis performance in the DBDP system. Due to the particle catalyst being attached to the surface of NiF, pieces of BMON can be easily separated from the solution and reused after a simple rinse. The excellent separation performance considerably eased recycle and reusing of the spent BMON. Fig. 10a presents MNZ removal efficiency over five reuse cycles in the DBDP system. The 125 min (5 × 25 min) MNZ elimination showed no apparent drop from the first to the fifth run, and the DBDP/BMON process could nearly completely degrade MNZ after five consecutive runs. After repeated use for 5 times, the removal efficiency of MNZ only decreased by 2.63%. The observation indicates that the DBDP process could regenerate BMON, granting it reusable catalysis activity in the DBDP system. Specifically, the dissolution of metal ions in the aqueous phase at weak acid pH met the permissible detection limit (GB3838–2002, China) by ICP-OES analysis. As shown in Fig. 10b, the highest ion concentrations of Bi Mn Ni in the DBDP/BMON process removing MNZ were 2 ng L^{-1}, 0.232 mg L^{-1}, and 0.036 mg L^{-1} could explain the high stability and reusability of BMON. The stability of BMON was shown in Fig. 10c and d via XRD diffraction.
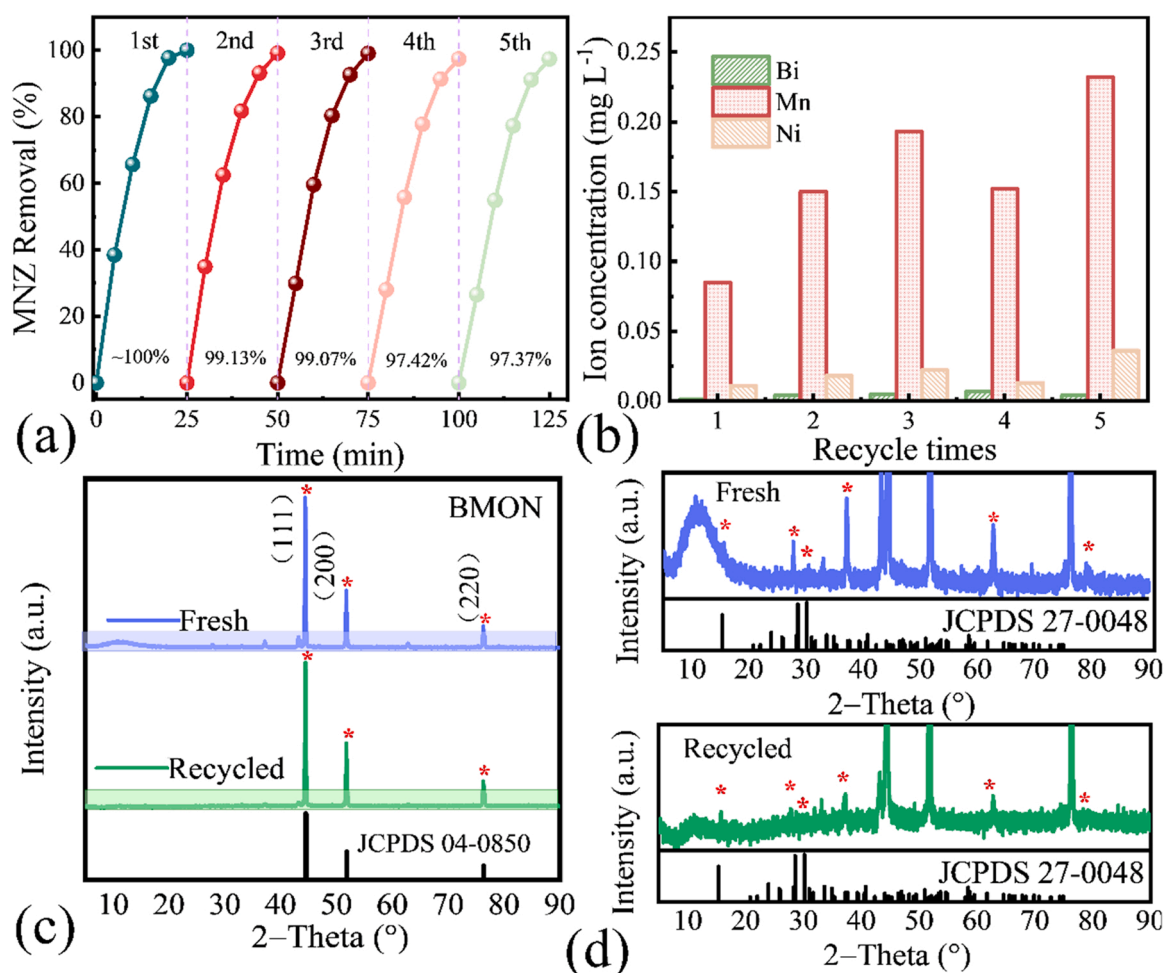

Fig. 10. Removal effect of continuous treatment of MNZ (a), and metal ion concentration in solution (b) in DBDP/BMON system (b) The XRD diffraction (c) and enlarged image (d) of fresh and recycled BMON. Reaction condition: V= 200 mL, [MNZ]= 10 mg L^{-1}, water circulation rate= 150 mL min^{-1}, input voltage= 18 kV.

The sharp crystal peaks indicated a high purity phase and comparing the fresh and recycled $Bi_2Mn_4O_{10}$, no apparent changes were observed, but the peak intensity was slightly weakened. The SME image in Fig. S9 shows the micromorphology of BMON recovered after 125 min of continuous catalysis. The overall structure of the NiF remains stable, with the Ni skeleton still supporting the $Bi_2Mn_4O_{10}$ catalyst loaded on the surface. However, $Bi_2Mn_4O_{10}$ no longer exists in the shape of a crystalline flower composed of stubby sticks and transformed into a finer rod-like structure that might be caused by the water flow and bubbles eroding. Generally, BMON could maintain the relative structure stability during the DBDP process, meanwhile maintaining the catalytic performance.

3.4. MNZ abatement in the DBDP/BMON process

3.4.1. Possible degradation mechanism analysis

Electrons can collide with the background molecular and produce large amounts of reactive species by bombardment, dissociation, etc. [61]. These reactive species or electrons can directly react and decompose with MNZ into smaller molecules. To investigate the role of reactive species in MNZ elimination, batches of scavenging were conducted

[62–64], and the corresponding results are shown in Fig. 11a and b. A significant inhibitory effect on MNZ removal was observed in the presence of p-BQ, the $O_2^{\bullet-}$ scavenger. As shown in Fig. S10, 99.26% of the initial MNZ was degraded after 25 min in the absence of scavengers, and 94.9%, 59.5%, 66.9%, and 63.0% were removed with the dosage of 0.1 mM IPA, p-BQ, $AgNO_3$, and FFA respectively. Illustrate the multifarious active species involved in the removal of MNZ. In addition, more obvious obstacles appeared to increase the addition of scavengers, especially in p-BQ dosage. A dramatic decrease in MNZ removal (from 59.5% to 6.0%) and removal rate (from 0.0340 min^{-1} to 0.0025 min^{-1}) were obtained with the p-BQ dosage increase from 0.1 mM to 10 mM. To reduce the trapping capability gap between different scavengers, hindrance efficiency (δ) is introduced to evaluate the scavenger obstructs the AOPs process and could be calculated as Eq. (15):

$$\delta(\%) = \frac{\xi_0 - \xi}{\xi_0} \times 100\% \tag{15}$$

where ξ_0 was the degradation efficiency when the scavenger was added at 0.1 mM, and ξ was the degradation efficiency when the scavenger was added at 5 mM. Based on the calculation results of δ, the contribution order of active species was $O_2^{\bullet-}$ (δ = 80.73%) > $^1O_2$ (δ = 67.05%) > $^{\bullet}OH$

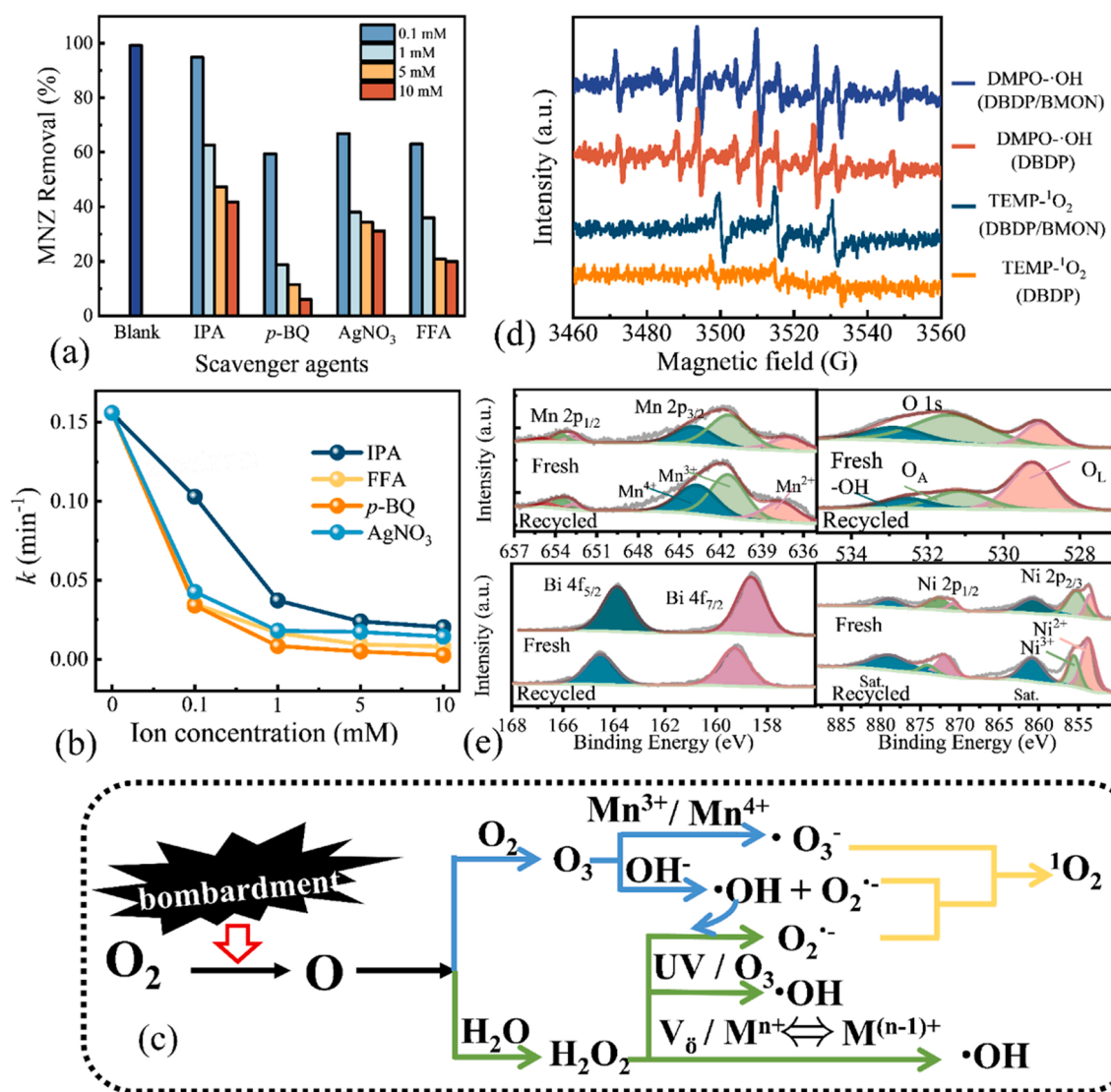**Fig. 11.** Scavenger effect on MNZ removal (a). ROS transformation in solution (b). Scavenger effect on MNZ removal rate (c).EPR spectra of DMPO-•OH and TEMP-$^1O_2$ adduct in the aqueous suspension (d) XPS spectra of BMON before and after use (e). reaction condition: V= 200 mL, [MNZ]= 10 mg L^{-1}, water circulation rate= 150 mL min^{-1}, input voltage= 18 kV.

($\delta = 50.07\%$) > e$^-$/H$^\bullet$ ($\delta = 48.63\%$). Compared with the presence of FFA and *p*-BQ, a more moderate decrease of removal effect was observed in IPA and AgNO$_3$ addition of 5 mM, and the decline was not significant. The phenomenon of scavenger experiments stresses the important contribution of O$_2^{\bullet-}$ and ^{1}O$_2$ to MNZ degradation in terms of quality and quantity.

The radical conversion in the DBDP/BMON system was complicated, as shown in Table S3 (Eqs. (S1)–(S25)), and for better understanding parts of them were concentrated on the reactions in aqueous and simplified in Fig. 11c [12,42,65–76]. During the discharge process, electron bombardment with the background molecules generates O$_3$ and H$_2$O$_2$, which were activated to radicals under the affection of catalyst and UV. Because of the thermodynamically favored (E_0, Mn^{4+}/ Mn^{3+} = 0.95 V; E_0, O$_2^{\bullet-}$/^{1}O$_2$ = −0.34 V), ^{1}O$_2$ was generated from a direct oxidation of O$_2^{\bullet-}$ by Mn^{4+} or a recombination of two superoxide radicals [77]. Particularly, ^{1}O$_2$ was transformed from O$_2^{\bullet-}$, explaining the reason that *p*-BQ had such a significant inhabitance on MNZ removal by hindering the production of both ^{1}O$_2$ and O$_2^{\bullet-}$. When the dosage of *p*-BQ and FFA were increased from 0.1 mM to 10 mM, the differences between their inhibition effect rose from 3.58% to 13.8%, suggesting that ^{1}O$_2$ played a significant role in the DBDP/BMON process. The generated O$_2^{\bullet-}$ was primarily consumed for ^{1}O$_2$ generation instead of directly contributing to MNZ degradation. The characteristic EPR spectra of DMPO-$^\bullet$OH and TEMP-^{1}O$_2$ in DBDP and DBDP/BMON systems were exhibited in Fig. 11d. Peaks separation of 45 Gauss and 30 Gauss further indicated the existence of $^\bullet$OH and ^{1}O$_2$. The increasing intensity implied an increase in the concentration of $^\bullet$OH and ^{1}O$_2$, which explained the BMON promoting the DBDP to degrade the MNZ process. Researchers have proposed that the redox reaction between Mn^{3+}/Mn^{4+} will activate O$_3$, generating the ^{1}O$_2$ [78]. Specifically, although IPA could block the effect of $^\bullet$OH, other pathways, especially the ^{1}O$_2$ and O$_2^{\bullet-}$ could continue working on MNZ degradation. The scavenge experiments showed the advantages of the DBDP system. Compared with other AOPs systems relying on single active species, DBDP/BMON could catalyze and produce multiple active species through different pathways simultaneously. In various active substances, the main contribution is ^{1}O$_2$, and O$_2^{\bullet-}$ played an essential role in the generation path of ^{1}O$_2$, which is also indispensable in the system.
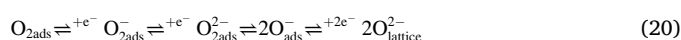
The further investigation of the effect of BMON in the DBDP process was by XPS to afford obvious evidence of surface information changes of BMON. As shown in Fig. 11e, all elements, including Mn 2p, O 1 s, Bi 4 f, and Ni 2p, are fitted and deconvoluted into different peaks. The Mn 2p spectra exhibit two peaks at 641.6 eV and 653.1 eV, corresponding to the binding energies of Mn 2p$_{3/2}$ and Mn 2p$_{1/2}$, with the spin-orbital splits of 11.5 eV, which matches the previously reported values [35, 38]. After further fitting, the Mn 2p spectrum could be divided into three peaks, of which the peaks at 642.4 eV, 641.2 eV, and 637.3 eV correspond to Mn^{4+}, Mn^{3+}, and Mn^{2+}, respectively [38,79]. The coexistence of Mn^{3+} and Mn^{4+} is essential for the catalytic activity of Bi$_2$Mn$_4$O$_{10}$. When the Vö is filled with adsorbed oxygen, a part of the oxygenated vacant Mn^{3+} neighbors will be oxidized into unstable Mn^{4+} to balance charge neutralization so that the sample surface produces more redox even active sites [79,80]. Due to Mn^{3+} being a redox couple in Mn^{3+}/Mn^{2+} and Mn^{3+}/Mn^{4+} as a reducing and oxidizable component, a high ratio of Mn^{3+} can enhance the transformation ability of Mn species between different valence states. A higher percentage of Mn^{3+}/Mn^{4+} in a certain range will bring better catalytic activity [30]. According to the relevant results, the relative contents of Mn^{3+} and Mn^{4+} in the freshly prepared BMON were approximately 52.6% and 29.6%, which suggested that the catalyst should have the potential for catalytic performance. Due to the essential catalysis capacity of Mn^{3+}, compared with the fresh BMON, the Mn^{3+} content in recycled BMON decreased from 45.7% to 34.0%. Noteworthy, compared with Bi$_2$Mn$_4$O$_{10}$, the peak of Mn^{2+} appeared in the BMON XPS spectrum, which stressed the effect of matrix Ni. Because the standard reduction potential of Mn^{4+}/Mn^{3+} (0.95 V), Mn^{4+}/Mn^{2+} (1.23 V), and Mn^{3+}/Mn^{2+} (1.51 V) are higher

than that of Ni^{2+}/Ni (−0.26 V), the reduction of Mn^{2+} by Ni is thermodynamically favorable. Thus, the content of Mn^{4+} decreased from 61.1% to 29.6%, and the content of Mn^{3+} and Mn^{2+} increased. As shown in Eqs. (16) and (17), the reduction of Mn^{4+} facilitates O$_3$ catalysis, based on the higher standard reduction potentials of O$_3$/O$_2$ (2.07 V), O$_3$ tends to be converted under the catalysis of low-price metal, and H$_2$O$_2$ could also be catalyzed to $^\bullet$OH [81,82].

The high-resolution O 1 s spectra of fresh BMON and recycled after oxidation were resolved into three individual peaks. For BMON, the deconvoluted peaks of -OH, O$_A$ (O^{2-}, derived from Vö), and O$_L$ center are around 532.83 eV, 531.34 eV, and 529.10 eV [36]. As shown in Table S1, O$_A$ reduced from 58.4% to 27.6%, and the relative intensity of O$_L$ increased from 21.6% to 58.5%. The content change between O$_A$ and O$_L$ might be associated with the catalysis effect of Mn (the transformation from Mn^{3+} to Mn^{4+}). Generally, Vö can be implied from the average oxidation state of Mn, which is created for charge balance as the presence of Mn^{3+}. Based on the reaction cycling of –Mn^{4+}–O^{2-}–Mn^{4+}– → –Mn^{3+}– Vö –Mn^{3+}– + 1/2 O$_2$ [46]. A similar phenomenon that the content of non-stoichiometric cerium (Ce^{3+}) is positively correlated with the concentration of surface Vö appeared in CeO$_2$ [36,83]. In addition, as shown in Eqs. (18) and (19), O$_L$ and Vö could participate in the generation of ROS during the DBDP process, causing the decrease of O$_A$ [42,84]. Trovarelli proposed that both superoxide and peroxides are intermediates in the general process of O$_2$ dissociation, leading to the incorporation of gas-phase O$_2$ into O$_L$ (Eq. (20)), corresponding to the XPS spectra [85]. Thus, given the changes in O$_L$ and O$_A$ content, it indicates that the surface O of BMON plays a specific role in the DBDP system.

The high-resolution XPS spectrum of Bi 4 f displays two strong peaks at 164.5 eV and 158.9 eV attributed to Bi 4 f$_{5/2}$ and 4 f$_{7/2}$, representing the presence of Bi-O [39,86]. The positive shift of Bi 4 f peaks demonstrated that Bi played the role of electron donor in the catalytic process. Consistent with the analysis by DFT calculation above, the electron cloud around Bi is less dense and tends to migrate. The two spin−orbit doublets of 855.4 eV and 873.1 eV are attributed to Ni 2p$_{3/2}$ and Ni 2p$_{1/2}$, respectively. Further deconvoluted into two peaks at 854.8 eV and 856.0 eV corresponds to Ni^{2+} and Ni^{3+}. As shown in Table S1, when BMON was recycled from the DBDP process, the content of Ni^{2+} increased from 32.5% to 67.5%, and Ni^{3+} decreased from 67.5% to 33.6%. To maintain the charge balance on the BMON surface, the Ni^{3+} in the catalyst accepted electrons from the O$_L$ and was reduced to Ni^{2+}, and the O$_L$ could be transformed to O$_2$, which completes the cycle of O$_{2ads}$/O$_L$, improving the catalytic efficiency [87]. Moreover, Ni^{2+} participates in the process of catalyzing H$_2$O$_2$ (Eqs. (21) and (22)), and the cycle of metal ion valence maintains the stability of the DBDP/BMON system [88].

According to the above discussion, the catalysis mechanism in the DBDP/BMON process was proposed. First, high voltage discharge triggered DBDP, producing ROS those could destroy the MNZ structure directly. Secondly, combined with BMON, H$_2$O$_2$ and O$_3$ were catalyzed by the cycle of M$^{(n+1)+}$/M^{n+} and O$_L$/V$_ö$, ^{1}O$_2$ and radicals generated began to work. Thirdly, to maintain the charge balance on the BMON surface, the Ni^{3+} in the catalyst accepts e$^-$ from the Vö and is reduced to Ni^{2+}, and the cycle of O$_L$/O$_2$ improves the catalytic efficiency. Moreover, O$_L$ was released in the form of ^{1}O$_2$ by transferring electrons from O$_2^{\bullet-}$ [87,89].

$$\equiv Mn^{n+} + O_3 + H_2O \rightarrow \ \equiv Mn^{n+1} + \bullet OH + O_2 + OH^- \ (n \leq 3) \tag{16}$$

$$Mn^{2+} + H_2O_2 \rightarrow Mn^{3+} + \bullet OH + OH^- \tag{17}$$

$$Oxygen \xrightarrow{\ V_ö\ } ROS \ species \tag{18}$$

$$O_L^- + O_2^{\bullet-} \rightarrow {}^1O_2 + O_L^{2-} \tag{19}$$

$$O_{2ads} \underset{}{\overset{+e^-}{\rightleftharpoons}} O_{2ads}^- \underset{}{\overset{+e^-}{\rightleftharpoons}} O_{2ads}^{2-} \rightleftharpoons 2O_{ads}^- \underset{}{\overset{+2e^-}{\rightleftharpoons}} 2O_{lattice}^{2-} \tag{20}$$

$$Ni^{2+} + H_2O_2 \rightarrow Ni^{3+} + \bullet OH + OH^- \tag{21}$$

$$Ni^{2+} + H_2O_2 \rightarrow Ni^{2+} + \bullet OH + \bullet OH \tag{22}$$

3.4.2. Possible degradation pathway of MNZ

A reasonable degradation pathway was essential for investigating MNZ abatement, as shown in Fig. S11. The peak at the retention time = 1.71 min represents the MNZ. With the processing time going by, the concentration of MNZ decreased, and other peaks of byproducts appeared, suggesting the MNZ structure was destroyed. Based on the ESI-QTOF-MS, DFT calculations, and related references [1,90–92], a possible degradation mechanism and pathway of MNZ were proposed. From the ESI-QTOF-MS results, 14 intermediates were detected within 25 min (Table S4), and DFT calculations were conducted to estimate the attacked position of the molecular. Fig. 12a and b display the MNZ analysis atomic serial number of bond population and Fukui function to calculate the strengths of bonds and radical attack sites in MNZ and its intermediates. In detail, compared to other bonds and atoms, N3-O2, N3-O3, C6-O1, and C5-N1 bonds (colored in blue) have smaller Mulliken population values and thus fracture easily. Atoms C(2), C(3), O(11) and O (12) (colored in purple) are more tend to be attacked by radicals and electrophilic groups more than atoms with smaller Fukui function values. As shown in Fig. 12c, those with high electron cloud density corresponds to the vulnerable attacked parts. As a result, 2-Methyl-4 (5)-nitroimidazole (P1), 1-(2-Hydroxyethyl)− 2-methyl-5--aminoimidazole (P2), 3-(2-hydroxyethyl)− 2-methylimidazol-4-ol (P3) and 2-Methyl-5-nitroimidazole-1-acetic acid (P4) may be generated (Fig. 13). Fig. S12 displays the relative contents of MNZ and its intermediates in the system. With the process of degradation, the MNZ content decreased gradually. In the first 15 min, P1 and P5 were the main degradation intermediates, indicating that MNZ→P1→P5→P11→P12 was the main degradation pathway. In the second half of discharge stage, the relative content of small molecule intermediates (P6, P7, P8, P9 and P12, etc.) began to increase, suggesting that pollutants were further destroyed.

Subsequently, C(4), O(7), and O(8) on P1 was attacked by radicals ($\bullet$OH and $O_2^{\bullet-}$) and electrophilic substance (O_3 and $^1O_2$) open imidazole ring and nitro reduction to generate P5 and P10. C(1), C(4), and N(7) with a high Fukui index on P2 were destroyed and transformed into P6, P7, and P11. Simultaneously, C(1), C(4), and O(7) on P3 were vulnerable to being further oxidized by radicals to generate P7 and P8 via ring opening and denitrification. Similarly, O(8), O(9), and O(13) on P4 through denitrification, hydroxyethyl cleavage generating P9 and P14. Finally, those intermediates with fewer carbon atoms via the broken chemical bonds were fragmented into small acids. In general, MNZ in the DBDP/BMON system might produce a series of imidazole, alcohol, and acid intermediates through denitrification, hydroxyethyl cleavage, nitro reduction, alcohol oxidation, and acetate cleavage. When the nitro group is removed, the atoms in the imidazole ring are vulnerable to attack, and the imidazole ring opening reaction might generate small organic acids.

3.4.3. Intermediate toxicity predictions

MNZ is usually applied as an antibiotic and antiprotozoal agent to prevent of systemic or local infections caused by anaerobic bacteria. As a clinical drug, MNZ is harmless to mammals under safe doses. However, the toxicity of its intermediates to aquatic organisms needs to be evaluated. Specifically, as an antibiotic, to assess the potential risk of antibiotic resistance genes (ARGs), the bioaccumulation factor of fish was also taken into consideration. The acute/chronic toxicity of MNZ and its intermediates were predicted to assess the ecological risk using the ECOSAR (version 2.2), and the bioaccumulation factor was calculated by T.E.S.T. (version 5.1.1) [93]. As shown in Fig. 14, the biological toxicity of P2, P3, and P5 is slightly enhanced. Still, as analyzed in the degradation pathway, the imidazole ring of denitration intermediates is more prone to be destroyed by the radicals' attack, resulting in less toxic products. Most intermediate products are non-acute toxic, and chronic toxicity has also decreased. From the perspective of species, the chronic impact on algae is the smallest, and the chronic toxicity to fish is smaller than that of daphnids due to the biomass. In addition, fish's declining bioconcentration factor also reduces the risk of food chain-induced ARGs. Consequently, DBDP/BMON process diminished the overall eco-risk of MNZ.

4. Conclusions

In this work, $Bi_2Mn_4O_{10}$/NiF was prepared via microwave and simply prepared and modified in catalyst stability and DBDP catalytic to construct an integrated DBDP/BMON system for MNZ pollutant control. The excellent pollutant elimination performance of the DBDP/BMON process could be summarized as follows: (i) DBDP generates H_2O_2, O_3, UV, $\bullet$OH, $^1O_2$, and $O_2^{\bullet-}$ et al. direct or indirect degradation of MNZ; (ii) BMON provides surface e^- and enhance $^1O_2$ yield via the redox between ternary metallic elements and $V_{\ddot{o}}$; (iii) MNZ was denitrification, hydroxyethyl cleavage, nitro reduction, alcohol oxidation, and acetate cleavage by ROS attacking, and finally transformed into fragment molecular. Therefore, the DBDP/BMON possessed significant applicability in the extensive pH range of 4–10 and performed well in anti-interference to coexisting substances. Meanwhile, the toxicity of
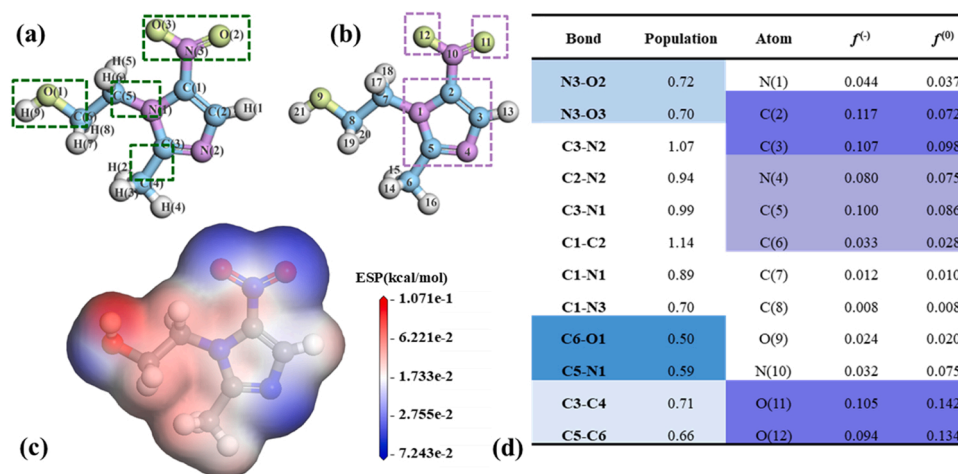

Bond	Population	Atom	$f^{(-)}$	$f^{(0)}$
N3-O2	0.72	N(1)	0.044	0.037
N3-O3	0.70	C(2)	0.117	0.072
C3-N2	1.07	C(3)	0.107	0.098
C2-N2	0.94	N(4)	0.080	0.075
C3-N1	0.99	C(5)	0.100	0.086
C1-C2	1.14	C(6)	0.033	0.028
C1-N1	0.89	C(7)	0.012	0.010
C1-N3	0.70	C(8)	0.008	0.008
C6-O1	0.50	O(9)	0.024	0.020
C5-N1	0.59	N(10)	0.032	0.075
C3-C4	0.71	O(11)	0.105	0.142
C5-C6	0.66	O(12)	0.094	0.134

Fig. 12. The MNZ analysis atomic serial number of bond population (a), Fukui function (b), Electrostatic potential distribution map (c), and Mulliken Population analysis and Fukui Function (d) of MNZ.
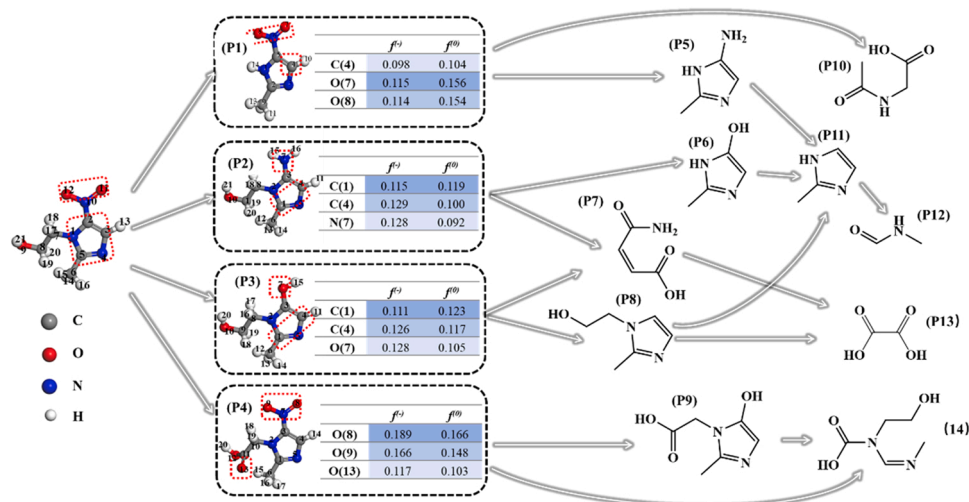
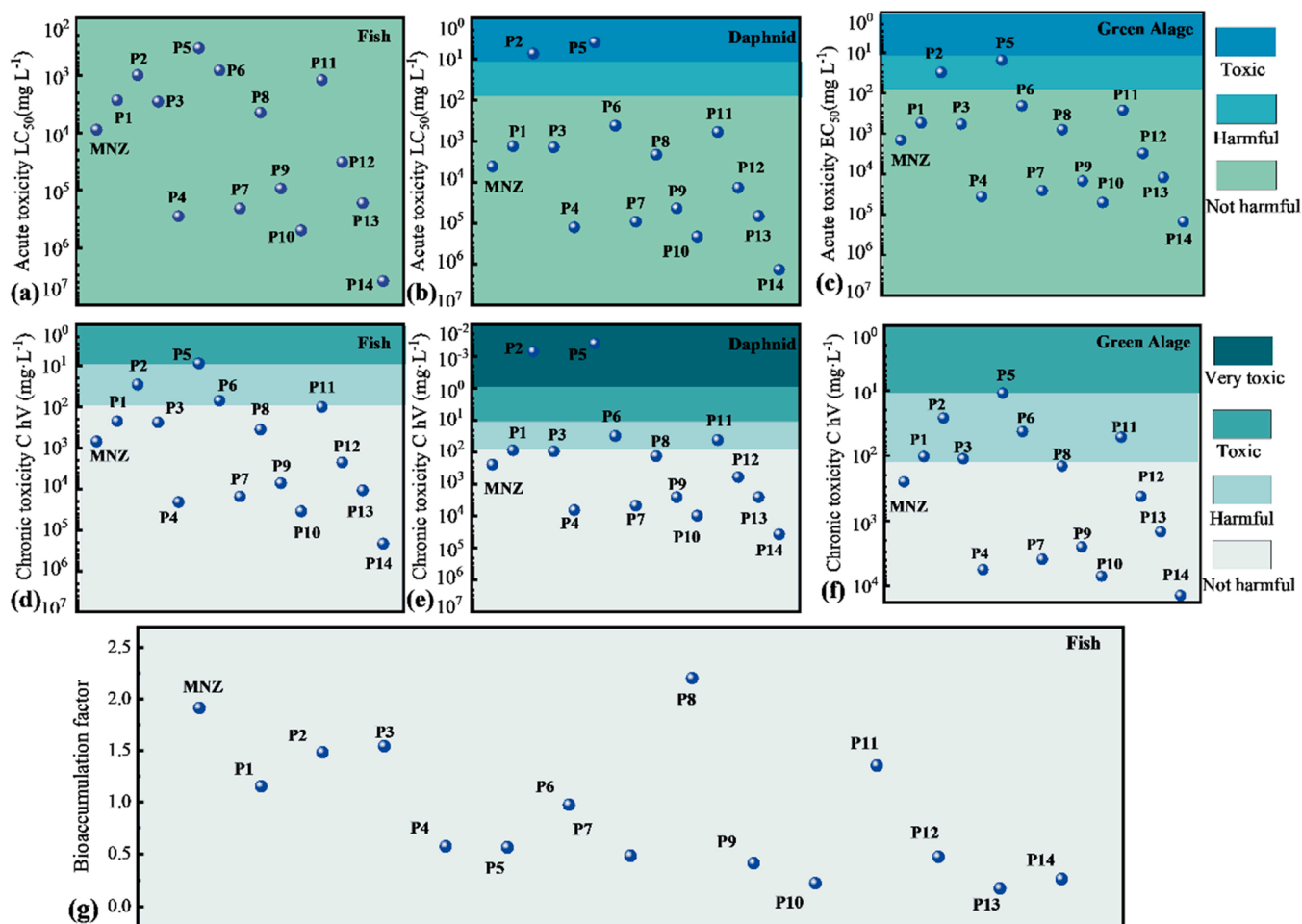**Fig. 13.** Possible degradation pathway of MNZ in DBDP/BMON process.

Fig. 14. Acute toxicity (a-c) and chronic toxicity (d-f) estimates of MNZ with its intermediate products during degradation by DBDP/BMON system via ECOSAR. Bioaccumulation factor (g) estimates of MNZ with its intermediate products during degradation by DBDP/BMON system via T.E.S.T.

intermediates was reduced, and the bioaccumulation was significantly reduced, in general. This study provides a promising preparation strategy in DBDP technology enhancement on water treatment by the active sites on BMON surface triggering ROS.

CRediT authorship contribution statement

Tianyao Shen: Conceptualization, Data curation, Formal analysis, Investigation, Methodology, Validation, Writing – original draft. **Xiaojing Wang:** Investigation, Writing – review & editing. **Jiaqin Li:**

Methodology, Investigation. **Peng Xu:** Data curation, Software. **Chunyan Yang**: Writing – review & editing. **Peng Wang:** Funding acquisition, Project administration, Resources, Supervision. **Guangshan Zhang:** Investigation, Methodology, Writing – review & editing, Funding acquisition.

Declaration of Competing Interest

The authors declare that they have no known competing financial interests or personal relationships that could have appeared to influence the work reported in this paper.

Data availability

Data will be made available on request.

Acknowledgments

Appendix A. Supplementary material

Supplementary data associated with this article can be found in the online version at doi:10.1016/j.apcatb.2023.122518.

References

[1] F. Görmez, Ö. Görmez, B. Gözmen, D. Kalderis, Degradation of chloramphenicol and metronidazole by electro-Fenton process using graphene oxide-Fe₃O₄ as heterogeneous catalyst, J. Environ. Chem. Eng. 7 (2019), 102990, https://doi.org/10.1016/j.jece.2019.102990.

[2] I. Saidi, I. Soutrel, D. Floner, F. Fourcade, N. Bellakhal, A. Amrane, F. Geneste, Indirect electroreduction as pretreatment to enhance biodegradability of metronidazole, J. Hazard. Mater. 278 (2014) 172–179, https://doi.org/10.1016/j.jhazmat.2014.06.003.

[3] P. Grenni, V. Ancona, A. Barra Caracciolo, Ecological effects of antibiotics on natural ecosystems: a review, Microchem. J. 136 (2018) 25–39, https://doi.org/10.1016/j.microc.2017.02.006.

[4] W. Cheng, M. Yang, Y. Xie, B. Liang, Z. Fang, E.P. Tsang, Enhancement of mineralization of metronidazole by the electro-Fenton process with a Ce/SnO₂-Sb coated titanium anode, Chem. Eng. J. 220 (2013) 214–220, https://doi.org/10.1016/j.cej.2013.01.055.

[5] A. Aboudalle, H. Djelal, F. Fourcade, L. Domergue, A.A. Assadi, T. Lendormi, S. Taha, A. Amrane, Metronidazole removal by means of a combined system coupling an electro-Fenton process and a conventional biological treatment: by-products monitoring and performance enhancement, J. Hazard. Mater. 359 (2018) 85–95, https://doi.org/10.1016/j.jhazmat.2018.07.006.

[6] J. Rivera-Utrilla, G. Prados-Joya, M. Sanchez-Polo, M.A. Ferro-Garcia, I. Bautista-Toledo, Removal of nitroimidazole antibiotics from aqueous solution by adsorption/bioadsorption on activated carbon, J. Hazard. Mater. 170 (2009) 298–305, https://doi.org/10.1016/j.jhazmat.2009.04.096.

[7] A.J. Watkinson, E.J. Murby, D.W. Kolpin, S.D. Costanzo, The occurrence of antibiotics in an urban watershed: from wastewater to drinking water, Sci. Total Environ. 407 (2009) 2711–2723, https://doi.org/10.1016/j.scitotenv.2008.11.059.

[8] N. Neghi, N.R. Krishnan, M. Kumar, Analysis of metronidazole removal and microtoxicity in photolytic systems: effects of persulfate dosage, anions and reactor operation-mode, J. Environ. Chem. Eng. 6 (2018) 754–761, https://doi.org/10.1016/j.jece.2017.12.072.

[9] D.H. Carrales-Alvarado, R. Ocampo-Perez, R. Leyva-Ramos, J. Rivera-Utrilla, Removal of the antibiotic metronidazole by adsorption on various carbon materials from aqueous phase, J. Colloid Interface Sci. 436 (2014) 276–285, https://doi.org/10.1016/j.jcis.2014.08.023.

[10] V. Balakumar, K. Sekar, C. Chuaicham, R. Manivannan, K. Sasaki, Synergistic ternary porous CN-PPy-MMt nanocomposite for efficient photocatalytic metronidazole mineralization: performance, mechanism, and pathways, Environ. Sci. Nano 8 (2021) 2261–2276, https://doi.org/10.1039/D1EN00254F.

[11] Z. Yang, A. Lai, H. Chen, Y. Yan, Y. Yang, W. Zhang, L. Wang, Degradation of metronidazole by dielectric barrier discharge in an aqueous solution, Front Environ. Sci. Eng. 13 (2019) 33–39, https://doi.org/10.1007/s11783-019-1117-4.

[12] M. Ansari, M. Sharifian, M.H. Ehrampoush, A.H. Mahvi, M.H. Salmani, H. Fallahzadeh, Dielectric barrier discharge plasma with photocatalysts as a hybrid emerging technology for degradation of synthetic organic compounds in aqueous environments: a critical review, Chemosphere 263 (2021), 128065, https://doi.org/10.1016/j.chemosphere.2020.128065.

[13] T. Shen, X. Wang, P. Xu, C. Yang, J. Li, P. Wang, G. Zhang, Effect of dielectric barrier discharge plasma on persulfate activation for rapid degradation of atrazine: optimization, mechanism and energy consumption, Environ. Res. (2022) 113287, https://doi.org/10.1016/j.envres.2022.113287.

[14] K. Shang, W. Li, X. Wang, N. Lu, N. Jiang, J. Li, Y. Wu, Degradation of p-nitrophenol by DBD plasma/Fe²⁺/persulfate oxidation process, Sep. Purif. Technol. 218 (2019) 106–112, https://doi.org/10.1016/j.seppur.2019.02.046.

[15] P. Xu, P. Wang, Q. Wang, R. Wei, Y. Li, Y. Xin, T. Zheng, L. Hu, X. Wang, G. Zhang, Facile synthesis of Ag₂O/ZnO/rGO heterojunction with enhanced photocatalytic activity under simulated solar light: kinetics and mechanism, J. Hazard. Mater. 403 (2021), 124011, https://doi.org/10.1016/j.jhazmat.2020.124011.

[16] K. Tian, L. Hu, L. Li, Q. Zheng, Y. Xin, G. Zhang, Recent advances in persulfate-based advanced oxidation processes for organic wastewater treatment, Chin. Chem. Lett. 33 (2022) 4461–4477, https://doi.org/10.1016/j.cclet.2021.12.042.

[17] C. Yang, P. Wang, J. Li, Q. Wang, P. Xu, S. You, Q. Zheng, G. Zhang, Photocatalytic PVDF ultrafiltration membrane blended with visible-light responsive Fe(III)-TiO₂ catalyst: degradation kinetics, catalytic performance and reusability, Chem. Eng. J. 417 (2021), 129340, https://doi.org/10.1016/j.cej.2021.129340.

[18] J. Ren, N. Jiang, K. Shang, N. Lu, J. Li, Y. Wu, Synergistic degradation of trans-ferulic acid by water falling film DBD plasma coupled with cobalt oxyhydroxide: Performance and mechanisms, Chem. Eng. J. 372 (2019) 321–331, https://doi.org/10.1016/j.cej.2019.04.147.

[19] X. Wang, P. Wang, X. Liu, L. Hu, Q. Wang, P. Xu, G. Zhang, Enhanced degradation of PFOA in water by dielectric barrier discharge plasma in a coaxial cylindrical structure with the assistance of peroxymonosulfate, Chem. Eng. J. 389 (2020), https://doi.org/10.1016/j.cej.2020.124381.

[20] K. Shang, W. Li, X. Wang, N. Lu, N. Jiang, J. Li, Y. Wu, Degradation of p-nitrophenol by DBD plasma/Fe²⁺/persulfate oxidation process, Sep. Purif. Technol. 218 (2019) 106–112, https://doi.org/10.1016/j.seppur.2019.02.046.

[21] C.R. Dela Cruz, B. Lorenz, Y.Y. Sun, Y. Wang, S. Park, S. Cheong, M.M. Gospodinov, C.W. Chu, Pressure-induced enhancement of ferroelectricity in multiferroicRMn₂O₅(R=Tb,Dy,Ho), Phys. Rev. B 76 (2007), https://doi.org/10.1103/PhysRevB.76.174106.

[22] Z.R. Kann, J.T. Auletta, E.W. Hearn, S. Weber, K.D. Becker, H. Schneider, M. W. Lufaso, Mixed crystal formation and structural studies in the mullite-type system Bi₂Fe₄O₉–Bi₂Mn₄O₁₀, J. Solid State Chem. 185 (2012) 62–71, https://doi.org/10.1016/j.jssc.2011.10.046.

[23] C. Li, S. Thampy, Y. Zheng, J.M. Kweun, Y. Ren, J.Y. Chan, H. Kim, M. Cho, Y. Y. Kim, J.W.P. Hsu, K. Cho, Thermal stability of mullite RMn₂O₅ (R = Bi, Y, Pr, Sm or Gd): combined density functional theory and experimental study, J. Phys. Condens. Matter 28 (2016), 125602, https://doi.org/10.1088/0953-8984/28/12/125602.

[24] W. Zhang, J. Chen, Y. Wang, L. Fan, J. Deng, R. Yu, X. Xing, Morphology evolution and physical properties of Bi₂Mn₄O₁₀ synthesized by hydrothermal method, J. Cryst. Growth 380 (2013) 1–4, https://doi.org/10.1016/j.jcrysgro.2013.05.025.

[25] C. Dong, Z. Qu, X. Jiang, Y. Ren, Tuning oxygen vacancy concentration of MnO₂ through metal doping for improved toluene oxidation, J. Hazard. Mater. 391 (2020), 122181, https://doi.org/10.1016/j.jhazmat.2020.122181.

[26] L. Li, J. Yan, T. Wang, Z.J. Zhao, J. Zhang, J. Gong, N. Guan, Sub-10 nm rutile titanium dioxide nanoparticles for efficient visible-light-driven photocatalytic hydrogen production, Nat. Commun. 6 (2015) 5881, https://doi.org/10.1038/ncomms6881.

[27] J. Yan, G. Wu, N. Guan, L. Li, Z. Li, X. Cao, Understanding the effect of surface/bulk defects on the photocatalytic activity of TiO2: anatase versus rutile, Phys. Chem. Chem. Phys. 15 (2013) 10978–10988, https://doi.org/10.1039/C3CP50927C.

[28] C. Bao, H. Wang, C. Wang, X. Zhang, X. Zhao, C. Dong, Y. Huang, S. Chen, P. Guo, X. She, Y. Sun, D. Yang, Cooperation of oxygen vacancy and Feᴵᴵᴵ/Feᴵᴵ sites in H₂-reduced Fe-MIL-101 for enhanced Fenton-like degradation of organic pollutants, J. Hazard. Mater. 441 (2023), 129922, https://doi.org/10.1016/j.jhazmat.2022.129922.

[29] I. Baidikova, H. Matralis, J. Naud, C. Papadopoulou, E.A. Mamedov, B. Delmon, Characterization of bismuth-manganese oxide catalysts for methane oxidative coupling, Appl. Catal. A Gen. 89 (1992) 169–182, https://doi.org/10.1016/0926-860X(92)80231-Z.

[30] L. Liu, J. Li, H. Zhang, L. Li, P. Zhou, X. Meng, M. Guo, J. Jia, T. Sun, In situ fabrication of highly active γ-MnO₂/SmMnO₃ catalyst for deep catalytic oxidation of gaseous benzene, ethylbenzene, toluene, and o-xylene, J. Hazard. Mater. 362 (2019) 178–186, https://doi.org/10.1016/j.jhazmat.2018.09.012.

[31] S.M. Robin, Spectrophotometric determination of hydrogen peroxide using potassium titanium(IV) oxalate, Analyst 105 (1980) 950–954, https://doi.org/10.1039/AN9800500950.

[32] G. Eisenberg, Colorimetric determination of hydrogen peroxide, Ind. Eng. Chem. Anal. Ed. 28101 (2011) https://doi.org/15(1943)327-328. 10.4236/ajac.

[33] S.B. Mathew, A.K. Pillai, V.K. Gupta, Spectrophotometric determination of hydrogen peroxide using leucocrystal violet in micellar medium, J. Dispers. Sci. Technol. 30 (2009) 609–612, https://doi.org/10.1016/S0003-2670(00)82563-5.

[34] W. Setyawan, S. Curtarolo, High-throughput electronic band structure calculations: challenges and tools, Comp, Mater. Sci. 49 (2010) 299–312, https://doi.org/10.1016/j.commatsci.2010.05.010.

[35] J. Zhan, Y. Long, Synthesis of $Bi_2Mn_4O_{10}$ nanoparticles and its anode properties for LIB, Ceram. Int. 44 (2018) 14891–14895, https://doi.org/10.1016/j.ceramint.2018.04.189.

[36] S. Ma, X. Wang, T. Chen, Z. Yuan, Effect of surface morphology on catalytic activity for NO oxidation of $SmMn_2O_5$ nanocrystals, Chem. Eng. J. 354 (2018) 191–196, https://doi.org/10.1016/j.cej.2018.07.197.

[37] X. Wang, P. Xu, C. Yang, T. Shen, J. Qu, P. Wang, G. Zhang, Enhanced 4-FP removal with $MnFe_2O_4$ catalysts under dielectric barrier discharge plasma: economical synthesis, catalytic performance and degradation mechanism, J. Hazard. Mater. 414 (2021), 125602, https://doi.org/10.1016/j.jece.2021.105160.

[38] W. Si, Y. Wang, Y. Peng, J. Li, Selective dissolution of A-site cations in ABO_3 perovskites: a new path to high-performance catalysts, Angew. Chem. Int. Ed. Engl. 54 (2015), 7954-7957. https://doi.org/10.1002/anie.201502632.

[39] C. Yang, H. Chai, P. Xu, P. Wang, X. Wang, T. Shen, Q. Zheng, G. Zhang, One-step synthesis of a 3D/2D Bi_2WO_6/g-C_3N_4 heterojunction for effective photocatalytic degradation of atrazine: kinetics, degradation mechanisms and ecotoxicity, Sep. Purif. Technol. 288 (2022), 120609, https://doi.org/10.1016/j.seppur.2022.120609.

[40] P. Guha, B. Mohanty, R. Thapa, R.M. Kadam, P.V. Satyam, B.K. Jena, Defect-engineered MoO2 nanostructures as an efficient electrocatalyst for oxygen evolution reaction, ACS Appl. Energy Mater., 3, 2020, pp. 5208–5218. 〈https://doi.org/10.1021/acsaem.9b02551〉.

[41] Y. Wang, R. Wang, L. Yu, Y. Wang, C. Zhang, X. Zhang, Efficient reactivity of $LaCu_{0.5}Co_{0.5}O_3$ perovskite intercalated montmorillonite and g-C_3N_4 nanocomposites in microwave-induced H_2O_2 catalytic degradation of bisphenol A, Chem. Eng. J. 401 (2020), 126057, https://doi.org/10.1016/j.cej.2020.126057.

[42] Y. Hao, Y. Ma, X. Zhang, J. Li, S. Wang, X. Chen, F. Li, Unraveling the importance between electronic intensity and oxygen vacancy on photothermocatalytic toluene oxidation over CeO_2, Chem. Eng. J. 433 (2022), 134619, https://doi.org/10.1016/j.cej.2022.134619.

[43] S. Lu, G. Wang, S. Chen, H. Yu, F. Ye, X. Quan, Heterogeneous activation of peroxymonosulfate by $LaCo_{1−x}Cu_xO_3$ perovskites for degradation of organic pollutants, J. Hazard. Mater. 353 (2018) 401–409, https://doi.org/10.1016/j.jhazmat.2018.04.021.

[44] J. Gao, C. Jia, L. Zhang, H. Wang, Y. Yang, S. Hung, Y. Hsu, B. Liu, Tuning chemical bonding of MnO_2 through transition-metal doping for enhanced CO oxidation, J. Catal. 341 (2016) 82–90, https://doi.org/10.1016/j.jcat.2016.06.009.

[45] K. Ye, K. Li, Y. Lu, Z. Guo, N. Ni, H. Liu, Y. Huang, H. Ji, P. Wang, An overview of advanced methods for the characterization of oxygen vacancies in materials, TrAC-Trend in, Anal. Chem. 116 (2019) 102–108, https://doi.org/10.1016/j.trac.2019.05.002.

[46] P. Wang, J. Zhao, Q. Zhao, X. Ma, X. Du, X. Hao, B. Tang, A. Abudula, G. Guan, Microwave-assisted synthesis of manganese oxide catalysts for total toluene oxidation, J. Colloid Interface Sci. 607 (2022) 100–110, https://doi.org/10.1016/j.jcis.2021.08.170.

[47] K. Zhu, F. Shi, X. Zhu, W. Yang, The roles of oxygen vacancies in electrocatalytic oxygen evolution reaction, Nano Energy 73 (2020), 104761, https://doi.org/10.1016/j.nanoen.2020.104761.

[48] H. Wang, J. Zhan, W. Yao, B. Wang, S. Deng, J. Huang, G. Yu, Y. Wang, Comparison of pharmaceutical abatement in various water matrices by conventional ozonation, peroxone (O_3/H_2O_2), and an electro-peroxone process, Water Res. 130 (2018) 127–138, https://doi.org/10.1016/j.watres.2017.11.054.

[49] X. Wang, P. Xu, C. Yang, T. Shen, J. Qu, P. Wang, G. Zhang, Enhanced 4-FP removal with $MnFe_2O_4$ catalysts under dielectric barrier discharge plasma: economical synthesis, catalytic performance and degradation mechanism, J. Hazard. Mater. 414 (2021), 125602, https://doi.org/10.1016/j.jhazmat.2021.125602.

[50] W. Yao, Q. Qu, U. von Gunten, C. Chen, G. Yu, Y. Wang, Comparison of methylisoborneol and geosmin abatement in surface water by conventional ozonation and an electro-peroxone process, Water Res. 108 (2017) 373–382, https://doi.org/10.1016/j.watres.2016.11.014.

[51] L. Hu, P. Wang, G. Liu, Q. Zheng, G. Zhang, Catalytic degradation of p-nitrophenol by magnetically recoverable Fe_3O_4 as a persulfate activator under microwave irradiation, Chemosphere 240 (2020), 124977, https://doi.org/10.1016/j.chemosphere.2019.124977.

[52] C. Wang, J. Zhang, J. Du, P. Zhang, Z. Zhao, W. Shi, F. Cui, Rapid degradation of norfloxacin by VUV/Fe^{2+}/H_2O_2 over a wide initial pH: process parameters, synergistic mechanism, and influencing factors, J. Hazard. Mater. 416 (2021), 125893, https://doi.org/10.1016/j.jhazmat.2021.125893.

[53] S. Giannakis, K.A. Lin, F. Ghanbari, A review of the recent advances on the treatment of industrial wastewaters by sulfate radical-based advanced oxidation processes (SR-AOPs), Chem. Eng. J. 406 (2021), 127083, https://doi.org/10.1016/j.cej.2020.127083.

[54] L. Hu, G. Zhang, M. Liu, Q. Wang, P. Wang, Enhanced degradation of Bisphenol A (BPA) by peroxymonosulfate with Co_3O_4-Bi_2O_3 catalyst activation: Effects of pH, inorganic anions, and water matrix, Chem. Eng. J. 338 (2018) 300–310, https://doi.org/10.1016/j.cej.2018.01.016.

[55] W. Qin, X. Yuan, L. Sun, Z. Qiang, D. Xia, Insights into the activation of ozonation by hydroxylamine: Influential factors, degradation mechanism and reaction kinetics, J. Hazard. Mater. 373 (2019) 600–607, https://doi.org/10.1016/j.jhazmat.2019.03.121.

[56] D. Zhu, Z. Sun, H. Zhang, A. Zhang, Y. Zhang, A.C. Miruka, L. Zhu, R. Li, Y. Guo, Y. Liu, Reactive nitrogen species generated by gas-liquid dielectric barrier discharge for efficient degradation of perfluorooctanoic acid from water, Environ.

[57] Z. Wang, R. Yuan, Y. Guo, L. Xu, J. Liu, Effects of chloride ions on bleaching of azo dyes by Co^{2+}/oxone reagent: kinetic analysis, J. Hazard. Mater. 190 (2011) 1083–1087, https://doi.org/10.1016/j.jhazmat.2011.04.016.

[58] D.B. Miklos, C. Remy, M. Jekel, K.G. Linden, J.E. Drewes, U. Hübner, Evaluation of advanced oxidation processes for water and wastewater treatment – a critical review, Water Res. 139 (2018) 118–131, https://doi.org/10.1016/j.watres.2018.03.042.

[59] P. Xu, P. Wang, X. Li, R. Wei, X. Wang, C. Yang, T. Shen, T. Zheng, G. Zhang, Efficient peroxymonosulfate activation by CuO-Fe_2O_3/MXene composite for atrazine degradation: performance, coexisting matter influence and mechanism, Chem. Eng. J. 440 (2022), https://doi.org/10.1016/j.cej.2022.135863.

[60] L. Hu, P. Wang, G. Zhang, G. Liu, Y. Li, T. Shen, J.C. Crittenden, Enhanced persulfate oxidation of organic pollutants and removal of total organic carbons using natural magnetite and microwave irradiation, Chem. Eng. J. 383 (2020), 123140, https://doi.org/10.1016/j.cej.2019.123140.

[61] X. Lu, G.V. Naidis, M. Laroussi, S. Reuter, D.B. Graves, K. Ostrikov, Reactive species in non-equilibrium atmospheric-pressure plasmas: generation, transport, and biological effects, Phys. Rep. 630 (2016) 1–84, https://doi.org/10.1016/j.physrep.2016.03.003.

[62] H. Wang, J. Zhang, P. Wang, L. Yin, Y. Tian, J. Li, Bifunctional copper modified graphitic carbon nitride catalysts for efficient tetracycline removal: synergy of adsorption and photocatalytic degradation, Chin. Chem. Lett. 31 (2020) 2789–2794, https://doi.org/10.1016/j.cclet.2020.07.043.

[63] D. Huang, X. Sun, Y. Liu, H. Ji, W. Liu, C. Wang, W. Ma, Z. Cai, A carbon-rich g-C_3N_4 with promoted charge separation for highly efficient photocatalytic degradation of amoxicillin, Chin. Chem. Lett. 32 (2021) 2787–2791, https://doi.org/10.1016/j.cclet.2021.01.012.

[64] J. Qu, X. Tian, X. Zhang, J. Yao, J. Xue, K. Li, B. Zhang, L. Wang, Y. Zhang, Free radicals-triggered reductive and oxidative degradation of highly chlorinated compounds via regulation of heat-activated persulfate by low-molecular-weight organic acids, Appl. Catal. B 310 (2022) 1, https://doi.org/10.1016/j.apcatb.2022.121359.

[65] X. Duan, H. Sun, Z. Shao, S. Wang, Nonradical reactions in environmental remediation processes: uncertainty and challenges, Appl. Catal. B 224 (2018) 973–982, https://doi.org/10.1016/j.apcatb.2017.11.051.

[66] S. Tang, D. Yuan, Y. Rao, M. Li, G. Shi, J. Gu, T. Zhang, Percarbonate promoted antibiotic decomposition in dielectric barrier discharge plasma, J. Hazard Mater. 366 (2019) 669–676, https://doi.org/10.1016/j.jhazmat.2018.12.056.

[67] Q. Wang, A. Zhang, P. Li, P. Héroux, H. Zhang, X. Yu, Y. Liu, Degradation of aqueous atrazine using persulfate activated by electrochemical plasma coupling with microbubbles: removal mechanisms and potential applications, J. Hazard. Mater. 403 (2021) 124087, https://doi.org/10.1016/j.jhazmat.2020.124087.

[68] T. Wang, G. Qu, J. Ren, Q. Yan, Q. Sun, D. Liang, S. Hu, Evaluation of the potentials of humic acid removal in water by gas phase surface discharge plasma, Water Res. 89 (2016) 28–38, https://doi.org/10.1016/j.watres.2015.11.039.

[69] M. Mehrjouei, S. Müller, D. Möller, A review on photocatalytic ozonation used for the treatment of water and wastewater, Chem. Eng. J. 263 (2015) 209–219, https://doi.org/10.1016/j.cej.2014.10.112.

[70] H. Kusic, N. Koprivanac, A.L. Bozic, Minimization of organic pollutant content in aqueous solution by means of AOPs: UV- and ozone-based technologies, Chem. Eng. J. 123 (2006) 127–137, https://doi.org/10.1016/j.cej.2006.07.011.

[71] N. Takeuchi, H. Mizoguchi, Study of optimal parameters of the H_2O_2/O_3 method for the decomposition of acetic acid, Chem. Eng. J. 313 (2017) 309–316, https://doi.org/10.1016/j.cej.2016.12.040.

[72] G. Merényi, J. Lind, S. Naumov, C. von Sonntag, The reaction of ozone with the hydroxide ion: mechanistic considerations based on thermokinetic and quantum chemical calculations and the role of HO_4^- in superoxide dismutation, Chem. Eur. J. 16 (2010) 1372–1377, https://doi.org/10.1002/chem.200802539.

[73] A. Cruz-Alcalde, S. Esplugas, C. Sans, Continuous versus single H_2O_2 addition in peroxone process: performance improvement and modelling in wastewater effluents, J. Hazard. Mater. 387 (2020), 121993, https://doi.org/10.1016/j.jhazmat.2019.121993.

[74] K. Zhang, A.P. Harvey, CO_2 decomposition to CO in the presence of up to 50% O_2 using a non-thermal plasma at atmospheric temperature and pressure, Chem. Eng. J. 405 (2021), 126625, https://doi.org/10.1016/j.cej.2020.126625.

[75] Y. Nosaka, A.Y. Nosaka, Generation and detection of reactive oxygen species in photocatalysis, Chem. Rev. 117 (2017) 11302–11336, https://pubs.acs.org/doi/10.1021/acs.chemrev.7b00161.

[76] Y. Kim, H. Lee, H. Oh, Z. Haider, J. Choi, Y. Shin, H. Kim, J. Lee, Revisiting the oxidizing capacity of the periodate-H_2O_2 mixture: identification of the primary oxidants and their formation mechanisms, Environ. Sci. Technol. 56 (2022) 5763–5774, https://pubs.acs.org/doi/10.1021/acs.est.1c08502.

[77] S. Zhu, X. Li, J. Kang, X. Duan, S. Wang, Persulfate activation on crystallographic manganese oxides: mechanism of singlet oxygen evolution for nonradical selective degradation of aqueous contaminants, Environ. Sci. Technol. 53 (2019) 307–315, https://pubs.acs.org/doi/10.1021/acs.est.8b04669.

[78] J. Ma, S. Zhang, X. Duan, Y. Wang, D. Wu, J. Pang, X. Wang, S. Wang, Catalytic oxidation of sulfachloropyridazine by MnO_2: effects of crystalline phase and peroxide oxidants, Chemosphere 267 (2021), 129287, https://doi.org/10.1016/j.chemosphere.2020.129287.

[79] X. Yang, C. Lai, L. Li, M. Cheng, S. Liu, H. Yi, M. Zhang, Y. Fu, F. Xu, H. Yan, X. Liu, B. Li, Oxygen vacancy assisted Mn-CuO Fenton-like oxidation of ciprofloxacin: Performance, effects of pH and mechanism, Sep. Purif. Technol. 287 (2022), 120517, https://doi.org/10.1016/j.seppur.2022.120517.

[80] C. Zhao, M. Yu, Z. Yang, J. Liu, S. Chen, Z. Hong, H. Chen, W. Wang, Oxygen reduction reaction catalytic activity enhancement over mullite $SmMn_2O_5$ via interfacing with perovskite oxides, Nano Energy 51 (2018) 91–101, https://doi.org/10.1016/j.nanoen.2018.06.039.

[81] S. Tian, J. Qi, Y. Wang, Y. Liu, L. Wang, J. Ma, Heterogeneous catalytic ozonation of atrazine with Mn-loaded and Fe-loaded biochar, Water Res. 193 (2021), 116860, https://doi.org/10.1016/j.watres.2021.116860.

[82] L. Li, S. Liu, M. Cheng, C. Lai, G. Zeng, L. Qin, X. Liu, B. Li, W. Zhang, Y. Yi, M. Zhang, Y. Fu, M. Li, M. Long, Improving the Fenton-like catalytic performance of $MnOx$-Fe_3O_4/biochar using reducing agents: a comparative study, J. Hazard. Mater. 406 (2021), 124333, https://doi.org/10.1016/j.jhazmat.2020.124333.

[83] J.M. López, A.L. Gilbank, T. García, B. Solsona, S. Agouram, L. Torrente-Murciano, The prevalence of surface oxygen vacancies over the mobility of bulk oxygen in nanostructured ceria for the total toluene oxidation, Appl. Catal. B 174–175 (2015) 403–412, https://doi.org/10.1016/j.jhazmat.2020.124333.

[84] S. Chen, D. Huang, L. Du, L. Lei, Y. Chen, G. Wang, Z. Wang, W. Zhou, J. Tao, R. Li, C. Zhou, Peroxymonosulfate activation by surface-modified bismuth vanadate for ciprofloxacin abatement under visible light: insights into the generation of singlet oxygen, Chem. Eng. J. 444 (2022), 136373, https://doi.org/10.1016/j.cej.2022.136373.

[85] A. Trovarelli, Catalytic properties of ceria and CeO_2-containing materials, Catal. Rev. 38 (1996) 439–520, https://doi.org/10.1039/C2CP42220D.

[86] J. Hu, G. Zhang, Q. Wang, Y. Sun, M. Liu, P. Wang, Facile synthesis of novel Co_3O_4-Bi_2O_3 catalysts and their catalytic activity on bisphenol A by peroxymonosulfate activation, Chem. Eng. J. 326 (2017) 1095–1104, https://doi.org/10.1016/j.cej.2017.05.168.

[87] H. Zeng, L. Deng, Z. Shi, J. Luo, J. Crittenden, Heterogeneous degradation of carbamazepine by Prussian blue analogues in the interlayers of layered double hydroxides: performance, mechanism and toxicity evaluation, J. Mater. Chem. A 7 (2019) 342–352, https://doi.org/10.1039/C8TA08801B.

[88] J. Kim, Y.J. Choe, S.H. Kim, S. Lee, S. Bhattacharjee, Grasping periodic trend and rate-determining step for S-modified metals of metal sulfides deployable to produce •OH via H_2O_2 cleavage, Appl. Catal. B 253 (2019) 60–68, https://doi.org/10.1016/j.apcatb.2019.04.016.

[89] Y. Ding, F. Yang, L. Zhu, N. Wang, H. Tang, Bi^{3+} self doped $NaBiO_3$ nanosheets: facile controlled synthesis and enhanced visible light photocatalytic activity, Appl. Catal. B 164 (2015) 151–158, https://doi.org/10.1016/j.apcatb.2014.09.019.

[90] A. Aboudalle, H. Djelal, L. Domergue, F. Fourcade, A. Amrane, A novel system coupling an electro-Fenton process and an advanced biological process to remove a pharmaceutical compound, metronidazole, J. Hazard. Mater. 415 (2021), 125705, https://doi.org/10.1016/j.jhazmat.2021.125705.

[91] J. Luo, Y. Yi, G. Ying, Z. Fang, Y. Zhang, Activation of persulfate for highly efficient degradation of metronidazole using Fe(II)-rich potassium doped magnetic biochar, Sci. Total Environ. 819 (2022), 152089, https://doi.org/10.1016/j.scitotenv.2021.152089.

[92] L. Xu, Y. Yang, W. Li, Y. Tao, Z. Sui, S. Song, J. Yang, Three-dimensional macroporous graphene-wrapped zero-valent copper nanoparticles as efficient micro-electrolysis-promoted Fenton-like catalysts for metronidazole removal, Sci. Total Environ. 658 (2019) 219–233, https://doi.org/10.1016/j.scitotenv.2018.12.040.

[93] J. Qu, Y. Xu, X. Zhang, M. Sun, Y. Tao, X. Zhang, G. Zhang, C. Ge, Y. Zhang, Ball milling-assisted preparation of N-doped biochar loaded with ferrous sulfide as persulfate activator for phenol degradation: multiple active sites-triggered radical/non-radical mechanism, Appl. Catal. B 316 (2022), 121639, https://doi.org/10.1016/j.apcatb.2022.121639.